MASTERARBEIT | MASTER'S THESIS

Titel | Title

Differentiable simulations of the cosmic microwave background

verfasst von | submitted by

Jeanne Eder BSc

angestrebter akademischer Grad | in partial fulfilment of the requirements for the degree of

Master of Science (MSc)

Wien | Vienna, 2025

Studienkennzahl lt. Studienblatt | Degree programme code as it appears on the student record sheet:	UA 066 861
Studienrichtung lt. Studienblatt | Degree programme as it appears on the student record sheet:	Masterstudium Astronomy
Betreut von | Supervisor:	Univ.-Prof. Dipl.-Phys. Dr. sc. ETH Oliver Hahn

Acknowledgements

First and foremost I want to thank my supervisor Professor Oliver Hahn for his unwavering support and invaluable guidance throughout this project. His enthusiasm, encouragement and appreciation of my progress made it easy to stay motivated - even during phases where I felt stuck.
Secondly, I would like to thank the entire cosmology research group for warmly welcoming me into the team. In particular, I am grateful to Lukas Winkler for helping with any technical or IT-related issues I encountered and to Thomas Floess for engaging with my project, offering valuable ideas and resources and providing encouragement along the way.
Finally I would like to thank my family, friends and my partner for their unwavering belief in me, especially during times when I struggled to believe in myself. Whether through kind words, shared laughter or simply being there, you helped me stay grounded and reminded me of my own strength.
Thank you, everyone!

Abstract

The Cosmic Microwave Background (CMB) is one of the most powerful probes of the early universe for describing, predicting and studying the evolution of density perturbations that seeded the large-scale structure observed today. The CMB is a relic radiation that was released in the early universe when photons decoupled from the primordial plasma. The observed anisotropies in the CMB temperature field, are small enough in amplitude to be accurately described using linear perturbation theory. In particular these perturbations are governed by the linearized Einstein-Boltzmann equations, a set of coupled partial differential equations that describe the evolution of metric and energy density fluctuations in a perturbed Friedmann-Lemaitre-Robertson-Walker (FLRW) universe.
Solving these equations requires a numerical Einstein-Boltzmann solver, such as the well established CAMB [1]. However, the Vienna cosmology group has developed their own Einstein-Boltzmann solver DISCO-EB [2], which is implemented in the JAX framework, a python library allowing for automatic differentiation. This makes the solver entirely differentiable and enables the possibility to assess the sensitivity of model predictions and observables to model parameters [3], making it a powerful tool for modern cosmological inference.
The thesis builds on the DISCO-EB framework to compute the angular temperature-temperature anisotropy power spectrum of the CMB. The main objective is to develop a robust and efficient numerical pipeline that takes the perturbation outputs from DISCO-EB and computes the observed temperature anisotropies through line-of-sight integration. Additionally, simulated anisotropy maps of the CMB sky are generated.

Kurzfassung

Die kosmische Mikrowellenhintergrundstrahlung (CMB) ist eines der leistungsfähigsten Tools zur Untersuchung des frühen Universums. Insbesondere spielt sie eine zentrale Rolle bei der Beschreibung und der Vorhersage der Entwicklung von Dichteperturbationen, aus denen die heute beobachtbaren großräumigen Strukturen hervorgegangen sind. Die kosmische Hintergrundstrahlung ist ein Relikt aus der Frühzeit des Universums und wurde in dem Moment freigesetzt, als sich Photonen vom primordialen Plasma entkoppelten. Die beobachtbaren Fluktuationen im Temperaturfeld der kosmischen Hintergrundstrahlung weisen eine so geringe Amplitude auf, dass sie im Rahmen der linearer Störungstheorie beschrieben werden können - mit den linearisierten Einstein-Boltzmann Gleichungen. Die Einstein-Boltzmann Gleichungen sind ein System partieller Differenzialgleichungen, das die Entwickung von Metrik und Energiedichtefluktationen in einem gestörten Friedmann-Lemaitre-Robertson-Walker (FLRW) Universum beschreibt.
Zur Lösung dieser Gleichung ist ein numerischer Einstein-Boltzmann Solver, wie zum Beispiel das ethablierte CAMB [1], erfoderlich. Die Kosmologiegruppe am Wiener Instituts für Astrophysik hat jedoch mit DISCO-EB [2] ihren eigenen Einstein-Boltzmann entwickelt, der vollständig im JAX-Framework implementiert ist. JAX ist eine Python-Bibliothek, die automatische Differenzierung unterstützt. Dadurch ist DISCO-EB vollständig differenzierbar und erlaubt eine effiziente Beurteilung der Sensitivität kosmologischer Observablen gegenüber den zugrundeliegenden Modellparametern [3]. Dies macht DISCO-EB zu einem wertvollen Tool für moderne kosmologische Inferenz.
Diese Arbeit basiert auf dem DISCO-EB Rahmenwerk und hat das Ziel das Temperaturanisotropiespektrum des CMB zu berechnen. Der Schwerpunkt liegt auf der Entwicklung einer numerischen Pipeline, die die von DISCO-EB berechhneten kosmologischen Perturbationen nutzt, um mittels einer Line-of-Sight Integration die beobachtbaren Temperaturanisotropien zu rekonstruieren. Darüber hinaus werden simulierte Anisotropiekarten des CMB-Himmels erzeugt.

Contents

List of Tables

List of Figures

Listings

1 Introduction

The Cosmic Microwave Background (CMB) is a faint, nearly uniform background of microwave radiation with a present-day temperature of approximately $T = 2.752\mathrm{K}$. It was emitted around 370 000 years after the Big Bang during an epoch of photon decoupling, when the universe cooled enough for electrons and protons to combine into neutral hydrogen. This allowed photons to travel freely for the first time, an event known as recombination. The CMB permeates the entire universe and can be observed in every direction, providing a snapshot of the universe at that early stage [5].

1.1 History

The discovery of the CMB marks one of the most significant events in the history of cosmology. It provided strong evidence for the Big Bang model and has since become a cornerstone in our understanding of the universe's origin, structure, geometry and composition [5].

1.1.1 First detection

The CMB was first detected in 1964 by the radio astronomers Arno Penzias and Robert Wilson at Bell Laboratories in Holmdel, New Jersey. They were observing the sky with a horn antenna, which is shown in Fig.1.1, a highly sensitive radio receiver originally designed for satellite communication. The horn antenna was considered the most advanced radio receiver of that time and used a cooling system with liquid Helium to restrict any possible inferences with the detectors internal radiation. While conducting their observations, they encountered a persistent, isotropic noise that was present both day and night across the entire sky. Despite extensive troubleshooting, they could not attribute the signal to any instrumental or environmental source [6].
Unknown to them, the concept of such a relic cosmic background radiation had already been theoretically predicted in 1941 by George Gamow and his collaborators. In 1964, Robert H. Dicke and Jim Peebles were preparing for the first systematic observational search for this relic radiation and had written a preprint paper describing their theoretical predictions [6].
After a call with Bernard Burke a professor at MIT, who was aware of Peebles and Dicke's preprint, Penzias and Wilson realized that the unexplained noise matched the theoretically predicted properties of this cosmic background radiation perfectly [6]. As a consequence, two papers were published side-by-side, one by Dicke, Peebles, Roll and Wilkinson titled "Cosmic Black-Body Radiation" [7] and one by Penzias and Wilson titled

"A Measurment of Excess Antenna Temperature at 4080 Mc/s" [8]. In 1978 Penzias and Wilson were awarded the Nobel prize for their groundbreaking discovery.

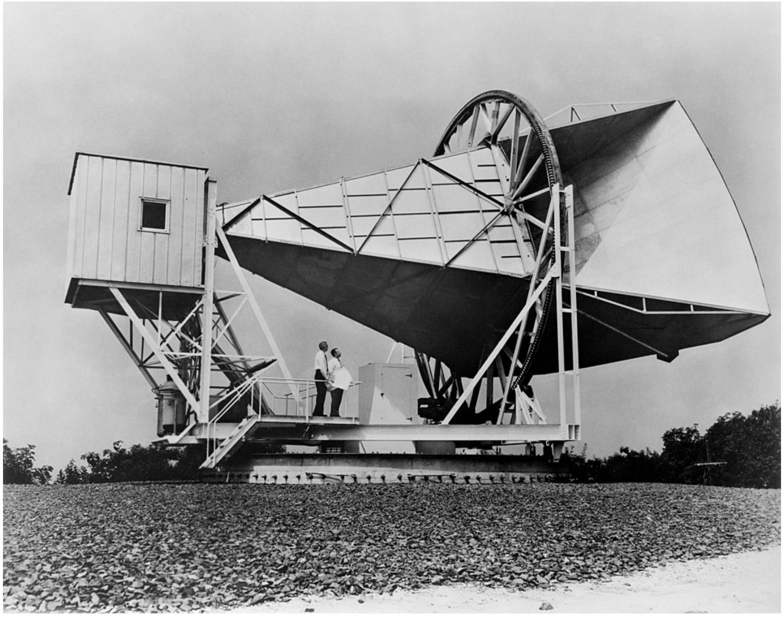

Figure 1.1: Radio telescope with Horn antenna in Holmdel New jersey with which the CMB was detected in 1964. (courtesy of NASA)

1.1.2 Modern Measurements

Since the discovery of the CMB by Penzias and Wilson, numerous ground-based, balloon-borne, and space-based experiments have been conducted to study the CMB. Among the most significant ones are the satellite missions COBE, WMAP and Planck [6].
The COsmic Background Explorer (COBE) satellite, launched in November 1989 by NASA, was the first mission to measure both the temperature anisotropies of the CMB and the spectrum. COBE's results marked the beginning of the era of precision cosmology, with increasing sensitivity for measurements [9]. Following COBE, DASI (Degree Angular Scale Interferometer) detected the first signs of CMB polarization [10], while CBI (Cosmic Background Imager) provided the first measurements of the E-mode polarization spectrum [11]. The Wilkinson Microwave Anisotropy Probe (WMAP) satellite and the Planck spacecraft then produced all-sky maps of the CMB with unprecedented precision capturing temperature and polarization anisotropies [9].

1.1.3 The impact of the CMB

As already mentioned, the discovery of the CMB revolutionized our understanding of the universe. First and foremost, the discovery of the CMB provided a very compelling piece of evidence for the Big Bang model. Opposed to the steady-state model, in the Big

Bang scenario the universe starts as a hot, dense initial state and has been expanding and cooling ever since, essentially predicting a relic radiation from this hot early state. The detection of the CMB strongly indicates that the early universe was significantly hotter and denser than presently, implying that the universe evolves over time rather than remaining static [6].
Furthermore, detailed measurements of the CMB have provided us with compelling evidence that the primordial fluctuations seen in the anisotropies have originated from quantum fluctuations magnified during an early phase of accelerated expansion known as inflation [5]. Moreover, the study of the CMB radiation and properties like its isotropy and temperature, has allowed to accurately determine the age of the universe which aligns well with other independent cosmological measurements. In addition, the CMB radiation provides a powerful tool for testing, constraining and improving the standard cosmological model. It has lead to numerous groundbreaking discoveries and continues to be one of the most valuable cosmological tools [12].

1.2 From perturbation theory to the CMB spectrum

1.2.1 Linear relativistic perturbation theory

The CMB is a powerful cosmological probe, primarily because its fluctuations were captured at a time when they were still small. This allows describing them to a high accuracy with linear perturbation theory, without the need to account for higher-order nonlinear effects. As a result, the underlying physics of the CMB can be derived from first principles and is governed by a well defined and understood set of equations, these equations are the so called Einstein-Boltzmann equations, which are a coupled set of partial differential equations. Here the Einstein equations describe the metric perturbations and the Boltzmann equation governs the evolution of various components of the universe such as baryonic and dark matter, radiation, dark energy and neutrinos, in the perturbed spacetime metric [5]. It is common to split the system into a linear and a non-linear part, since solving the full Einstein-Boltzmann equations is computationally demanding [3]. These CMB fluctuations are typically studied using statistical methods, especially by analyzing correlations between the temperature anisotropies, including the characteristic hot and cold spots [5].

Gauge Convention

In relativistic perturbation theory, which is essential for describing CMB anisotropies, the metric perturbations are no longer uniquely defined as in the classical Newtonian framework. Instead, they now depend on the choice of gauge, which refers to the coordinate system used to describe the perturbations. When choosing a different coordinate system, the values of the perturbation variables can change, and if not careful, fictitious perturbations might be introduced that can lead to fluctuations even in a perfectly homogeneous universe. This issue is known as the Gauge problem and a common approach to address

it is to adopt a convenient gauge and carefully track all metric and matter perturbations within that framework[5].
In this work, the synchronous gauge is adopted, as it is the most commonly used gauge in cosmological perturbation theory. It was first introduced by Lifshitz in 1964. In the synchronous gauge the time-time and time-space components of the metric perturbation vanish, simplifying some aspects of the Einstein equations [13].

The Einstein equations

The perturbed Friedmann-Lemaitre-Walker metric (FLRW) in the synchronous gauge takes the form of Eq.1.1

$$ds^2 = a^2(\eta)\{-d\eta^2 + (\delta_{ij} + h_{ij})dx^i dx^j\} \tag{1.1}$$

Here h_{ij} is the metric perturbation and δ_{ij} the Kronecker delta [13]. The metric perturbation h_{ij} can be decomposed into scalar, vector and tensor components through a scalar-tensor-vector decomposition. This can be written as Eq.1.2 [13].

$$h_{ij} = \frac{1}{3}h\delta_{ij} + \left(\partial_i\partial_j - \frac{1}{3}\delta_{ij}\nabla^2\mu\right) + (\partial_i A_j + \partial_j A_i) + h_{ij}^T \tag{1.2}$$

Here $h = h_{ii}$ is the trace part, μ is a scalar field that characterizes the traceless scalar part, A_i is a divergenceless vector field describing the vector mode and h_{ij}^T is the transverse and traceless tensor mode. Since we're mostly interested in scalar perturbations in this work, the scalar mode of h_{ij} can be written as a Fourier Integral as Eq.1.3 [13].

$$h_{ij}(\vec{x},\eta) = \int d^3k e^{i\vec{k}\vec{x}}\left[\hat{k}_i\hat{k}_j\boldsymbol{h}(\vec{k},\eta) + \left(\hat{k}_i\hat{k}_j - \frac{1}{3}\delta_{ij}\right)6\boldsymbol{\eta}(\vec{k},\eta)\right] \tag{1.3}$$

Here $\boldsymbol{h}(\vec{k},\eta)$ and $\boldsymbol{\eta}(\vec{k},\eta)$ are two scalar fields and k_i and k_j are derivatives of the Fourier modes. To avoid confusion with the conformal time η, the scalar potentials $\boldsymbol{h}$ and $\boldsymbol{\eta}$ are written in bold writing in this work.
The Einstein equations in a homogeneous FLRW universe which is described by the metric given in Eq.1.1 are shown in Eq.1.4 and 1.5, where $\bar{\rho}$ is the energy density, $\bar{P}$ the pressure, a the scale factor and η the conformal time. Here $' = \frac{d}{d\eta}$ [13].

$$\left(\frac{a'}{a}\right)^2 = \frac{8\pi}{3}Ga^2\bar{\rho} - \kappa \tag{1.4}$$

$$\frac{d}{d\eta}\left(\frac{a'}{a}\right) = -\frac{4\pi}{3}Ga^2(\bar{\rho} + 3\bar{P}) \tag{1.5}$$

The time-time, longitudinal time-space, trace space-space and longitudinal traceless space-space part of the linearized Einstein equations in Fourier space are known as Eq.1.9, where they are defined by the two scalar potentials $\boldsymbol{h}$ and $\boldsymbol{\eta}$ [13].

$$\frac{1}{2}\mathcal{H}\boldsymbol{h}' - k^2\boldsymbol{\eta} = 4\pi G a^2 \delta T^0_0, \tag{1.6}$$

$$k^2\boldsymbol{\eta}' = 4\pi G a^2(\rho + P)\theta, \tag{1.7}$$

$$\boldsymbol{h}'' + 2\mathcal{H}\boldsymbol{h}' - 2k^2\boldsymbol{\eta} = -8\pi G a^2 \delta T^i_i, \tag{1.8}$$

$$\boldsymbol{h}'' + 6\boldsymbol{\eta}'' + 2\mathcal{H}\boldsymbol{h}' + 6\mathcal{H}\boldsymbol{\eta}' - 2k^2\boldsymbol{\eta} = -24\pi G a^2(\rho + P)\sigma. \tag{1.9}$$

Here T is the energy momentum tensor [13].

The Boltzmann equation

The phase space distribution is defined as Eq.1.10, which consists of a zeroth-order distribution f_0 contributing only to the background and a perturbed piece Ψ in variables q and n_j, where $q_j = ap_j$ is a replacement for the pressure P and n_j is the direction vector [13].

$$f(x^i, P_j, \eta) = f_0(q)[1 + \Psi(x, q.n_j, \eta)] \tag{1.10}$$

Here f_0, as shown in Eq.1.11, is defined as the Fermi-Dirac distribution for fermions (+ sign) and the Bose-Einstein distribution for bosons (- sign) with $\epsilon = a(p^2 + m^2)^{1/2}$, $T_0 = aT$ the temperature of the particles today, g_s the number of spin degrees of freedom, h_P the Planck constant and k_B the Boltzmann constant [13].

$$f_0 = \frac{g_s}{h_P^3}\frac{1}{e^{\epsilon/k_B T} \pm 1} \tag{1.11}$$

The phase space distribution f evolves according to the Boltzmann equation Eq.1.12 [13]

$$\frac{Df}{d\eta} = \frac{\partial f}{\partial \eta} + \frac{dx^i}{d\eta}\frac{\partial f}{\partial q} + \frac{dq}{\partial \eta}\frac{\partial f}{\partial q} + \frac{dn_i}{d\eta}\frac{\partial f}{\partial n_i} = \left(\frac{\partial f}{\partial \eta}\right)_C \tag{1.12}$$

The Boltzmann equation in the synchronous gauge in Fourier space is then described as Eq.1.13 [13]

$$\frac{\partial \boldsymbol{\Psi}}{\partial \eta} + i\frac{q}{\epsilon}(\vec{k} + \hat{n})\boldsymbol{\Psi} + \frac{d\ln f_0}{d\ln q}\left[\boldsymbol{\eta}' - \frac{h' + 6\boldsymbol{\eta}'}{2}(\hat{k}\cdot\hat{n})^2\right] = \frac{1}{f_0}\left(\frac{\partial f}{\partial \eta}\right)_C \tag{1.13}$$

CMB Spectrum

The fluctuations in the CMB radiation arise from perturbations in the photon phase space distribution f. These perturbations can be determined by solving the Boltzmann equation and are conveniently expressed in terms of the photon brightness temperature perturbation $\Delta = \Delta T/T$ which is directly related to the perturbation in the distribution function f as shown in Eq.1.14.

$$f(x^i, q, n_j, \eta) = f_0\left(\frac{q}{1 + \Delta(x^i, q, n_j, \eta)}\right) \tag{1.14}$$

Here q refers to the co-moving momentum and is defined as $q = \epsilon$. This relates f and T, as perturbations in the distribution function correspond to local temperature variations while maintaining the Planck like shape of the CMB spectrum [13]. Using Eq.1.10, this leads to Eq.1.15 [13].

$$\Delta = -\left(\frac{d\ln f_0}{d\ln q}\right)^{-1}\Psi \tag{1.15}$$

Since both the gravitational source term and the linearized Thomson scattering collision term in the Boltzmann equation for Ψ show a proportionality to $\frac{d\ln f_0}{d\ln q}$, the momentum dependence cancels out. As a result, Δ becomes independent of the comoving momentum q. This implies, that the perturbed CMB radiation retains a Planck spectrum, with the brightness temperature at a given point in spacetime depending only on the photon propagation direction direction $\hat{n}$ [13]. In order to compute the CMB anisotropy at a given point in spacetime (x^i, η), the plane-wave contributions are superposed, which gives Eq. 1.16 with P_l being the Legendre polynomials and the multipole coefficients $\Delta_l = \frac{1}{4}F_{\gamma l}$ with $F_{\gamma l}$ being the Boltzmann moments [13].

$$\Delta(\vec{x},\hat{n},\eta) = \int d^3k e^{-i\vec{k}\vec{x}}\Delta(\vec{k},\hat{n},\eta) = \int d^3k e^{-i\vec{k}\vec{x}}\sum_{l=0}^{\infty}(-i)^l(2l+1)\Delta_l(\vec{k},\eta)P_l(\hat{k}\cdot\hat{\eta}) \tag{1.16}$$

The first step equality represents a Fourier transform, expressing the spatial dependence of Δ as a superposition of plane-wave modes. The second equality expands the angular dependence of $\Delta(\vec{k},\hat{n},\eta)$ in terms of the Legendre polynomials $P_l(\hat{k}\cdot\hat{\eta})$, which reflect the angular structure of the temperature anisotropies with respect tot the wavevector direction $\vec{k}$ [13]. This anisotropy is then expanded into spherical harmonics as in Eq.1.17 [13] with the spherical harmonics coefficient defined as Eq.1.18 and Δ_l being the anisotropy coefficient.

$$\Delta(\hat{n}) = \sum_{l=0}^{\infty}\sum_{m=-l}^{l} a_{lm}Y_{lm}(\hat{n}) \tag{1.17}$$

$$a_{lm} = (-i)^l 4\pi \int d^3k Y^*_{lm}(\hat{n})\Delta_l(\vec{k},\eta) \tag{1.18}$$

From that the angular power spectrum of the anisotropy can be calculated as the covariance matrix of the spherical harmonics coefficients as in Eq.1.19.

$$\langle a_{lm}a^*_{l'm'}\rangle = C_l\delta_{ll'}\delta_{mm'} \tag{1.19}$$

This relates to the angular two-point correlation function as Eq.1.20 [13].

$$C(\theta) = \langle\Delta(\hat{n_1})\Delta(\hat{n_2})\rangle = \frac{1}{4\pi}\sum_{l=0}^{\infty}(2l+1)C_lP_l(\hat{n_1}\cdot\hat{n_2}) \tag{1.20}$$

The anisotropy coefficient Δ_l, which is essentially the solution of the Boltzmann equation, can be written in terms of the metric potential $\psi_i(k)$ as Eq.1.21 [13].

$$\Delta_l(\vec{k}\eta) = \psi_i(\vec{k})\Delta_l(k,\eta) \tag{1.21}$$

Using the two point correlation function of the metric potential Eq.1.22, where P_ϕ corresponds to the primordial spectrum of curvature fluctuations and δ_D being the Dirac delta function, the final expression to calculate the CMB angular power spectrum is Eq.1.23 [13].

$$\langle \phi_i(\vec{k_1}) \phi_i(\vec{k_2}) \rangle = P_\phi \delta_D(\vec{k_1} + \vec{k_2}) \tag{1.22}$$

$$C_l = 4\pi \int d^3k P_\phi(k) \Delta^2(k, \eta) \tag{1.23}$$

1.3 DISCO-DJ

To compute the CMB power spectrum, the linearized Einstein-Boltzmann equations have to be solved for all relevant perturbations. This is typically done using a numerical Einstein-Boltzmann solver. Several well established Einstein-Boltzmann solver codes exist for this purpose with various levels of complexity, the most notable ones used in the cosmological community are CAMB [1] and CLASS [14].
These solvers offer robust and accurate predictions, however, none of them are differentiable. The Vienna cosmology group has therefore developed DISCO-DJ, a fully differentiable Einstein Boltzmann solver for cosmology implemented using JAX, a python library enabling automatic differentiation. With JAX it is possible to compute the Jacobian matrix of all solver outputs with respect to the input cosmological parameters. Additionally, JAX is optimized for execution on graphics processing units (GPUs), which significantly accelerates the solving of the Einstein-Boltzmann system [3].

1.3.1 Automatic Differentiation

Automatic differentiation is a method for computing exact derivatives and has recently emerged as a powerful third approach alongside the two common methods of computer-aided differentiation. Usually derivatives are either computed through symbolic differentiation, which relies on algorithms applying analytical derivation rules to derive exact expression for derivatives. While accurate, this method can produce very long expressions for complex functions, making the code less computationally efficient. Another way to compute derivatives, is using numerical differentiation, which is based on calculating finite differences. This approach is easy to implement and broadly applicable, however, it is an approximate method that can lead to higher-order derivatives becoming unstable and noisy [3].
Automatic differentiation takes advantage of the fact, that any computer program evaluating a mathematical expression can be treated as a nested sequence of elementary operations such as summation, multiplication and basis functions, whose derivatives are known. The derivative of the full expression is then computed by systematically applying the chain rule. When this is done by propagating derivatives from input to output alongside function values, the approach is known as forward-mode differentiation [3].

1.3.2 JAX

JAX is a Python library designed for high-performance numerical computing. It is based on array operations and supports automatic differentiation, which allows for creating fully differentiable codes in Python. JAX also supports just in time (JIT) compilation, which allows codes to be efficiently compiled and executed on GPUs. JAX has rapidly gained popularity in the cosmology community and therefore is expanding constantly [3].

1.4 This work

The DISCO-EB code is currently a minimal implementation of a differentiable Einstein-Boltzmann solver and there remains significant room for further development. Future extensions could include support for alternate models of dark energy, modified gravity, or other non-standard physics. Additionally, new deliverables such as the CMB anisotropy spectrum and the lensing potential can be incoperated in the framework [3].
This project contributes to that development. Its primary goal is to utilize the output of DISCO-EB, so the time evolved perturbations, to compute the temperature anisotropies observed in the CMB and to develop a numerical code in the JAX framework that achieves this to add to the current implementation of DISCO-EB. The first step in doing so is to compute the temperature-temperature angular power spectrum C_l^{TT} of the CMB and then to produce Gaussian realizations of these temperature anisotropies with the code created.

2 Methods

2.1 Background cosmological model

The first step in studying the cosmic microwave background is to establish the background cosmology. The background is governed by the cosmological principle, which states that the spatial distribution of matter is assumed to be isotropic and homogeneous on sufficiently large scales [15].
For the DISCO-EB code a flat extended ΛCDM cosmology is chosen as a background framework. The extensions to the standard ΛCDM model include the incorporation of massive neutrinos and a dynamical dark energy fluid whose equation of state is given by the Chevallier-Polarski-Linder parametrisation shown in Eq.2.1 [16].

$$w_{DE} = p/\rho = w_0 + w_a(1-a) \tag{2.1}$$

Where $w_0 = -0.99$ and $w_a = 0.0$ are fixed parameters and the dependence of a allows a time-varying dark energy equation of state. The total energy content considered in this model includes baryonic matter, cold dark matter, photons, massless neutrinos, massive neutrinos, and a quintessence-like dark energy component with a time-varying equation of state[3].
The set of cosmological parameters chosen are shown in Tab.2.1 which is taken from [3].

Parameter	Value	Meaning
Ω_K	0.0	Curvature density parameter
Ω_b	0.0488911	Baryon density parameter
Ω_m	0.3099	Matter density parameter
h	0.6742	Hubble parameter
n_s	0.96822	Primodrial spectral index
A_s	$2.1064 \cdot 10^{-9}$	Amplitude at $k_p = 0.05\mathrm{Mpc}^{-1}$
N_{eff}	3.046	Effective number of ultrarelativistic species
m_ν	0.06 eV	Mass of neutrino
w_0	-0.99	Dark energy equation of state parameter
w_a	0.0	Dark energy equation of state parameter
c_a^2	1.0	Dark energy sound speed
Y_{He}	0.284	Primordial Helium fraction
T_{CMB}	2.7255 K	CMB temperature today

Table 2.1: Cosmological parameters from PLANCK2018 [4] $EE+BAO+SN$ taken from [3]

Time variable

A common way to quantify time in cosmology, is by using the conformal time η, which provides a convenient framework for describing the evolution of the universe.
The conformal time is defined as Eq. 2.2.

$$\eta(a) = \int_0^a \frac{da'}{a'\mathcal{H}} \tag{2.2}$$

where $\mathcal{H} = aH$ is the conformal Hubble parameter [17].
Conformal time is related to the physical cosmic time t through Eq.2.3.

$$\frac{dt}{d\eta} = a \tag{2.3}$$

Cosmic Expansion and the Friedmann equation

The expansion history of the universe and with that the evolution of the scale factor $a(\eta)$ is governed by the Friedmann equation, which relates the Hubble parameter to the energy content of the universe.
The conformal Friedmann equation goes as Eq.2.4.

$$\mathcal{H} = \frac{1}{a}\frac{da}{d\eta} = \frac{a'}{a} = \sqrt{\frac{8\pi G\bar{\rho}}{3}} \tag{2.4}$$

where ρ is the background energy density. In natural units where $8\pi G = 1$, this equation simplifies to Eq.2.5.

$$\frac{a'}{a} = \sqrt{\frac{\bar{\rho}}{3}} \tag{2.5}$$

Here $\bar{\rho}$ is the total energy density expressed in units of $1/\mathrm{Mpc}^2$ and is given by Eq.2.6. The terms correspond to the different energy components of the universe. All the following equations are taken directly from the source code of DISCO-EB [2].

$$\bar{\rho} = \frac{\bar{\rho}_m \Omega_m}{a} + \frac{(\bar{\rho}_\gamma + \bar{\rho}_r)(N_{\mathrm{eff}} + N_{m\nu}\bar{\rho}_\nu)}{a^2} + \bar{\rho}_m \Omega_{\mathrm{DE}} \rho_Q a^2 + \bar{\rho}_m \Omega_K \tag{2.6}$$

The first term corresponds to the matter content of the universe, where $\bar{\rho}_m$ is known to be Eq.2.7.

$$\bar{\rho}_m = \frac{8\pi G \rho_{\mathrm{crit}}}{c^2} = 3.3.33795017 \cdot 10^{-11} H_0^2 \tag{2.7}$$

Here ρ_{crit} is the critical density today, which is defined as Eq.2.8.

$$\rho_{\mathrm{crit}} = \frac{3H_0^2}{8\pi G} \tag{2.8}$$

The second term corresponds to the radiation content of the the universe, containing of photons $\bar{\rho}_\gamma$, massless neutrinos $\bar{\rho}_r$ and massive neutrinos ρ_ν. Here the photon energy density $\bar{\rho}_\gamma$ is Eq 2.9.

$$\bar{\rho}_\gamma = 1.49594245 \cdot 10^{-13} T_{\mathrm{cmb}}^4 \tag{2.9}$$

$\bar{\rho}_r$, which is referring to the massless neutrino density per flavor is known to be Eq.2.10.

$$\bar{\rho}_r = 3.39739477 \cdot 10^{-14} T_{\text{cmb}}^4 \tag{2.10}$$

And $\bar{\rho}_\nu$, which is the massive neutrino density per flavor is known to be Eq.2.11.

$$\bar{\rho}_\nu = w \cdot \frac{1}{v(q)} \tag{2.11}$$

where $v(q) = \frac{1}{\sqrt{1+(a \cdot am_\nu/q)^2}}$ with q being the comoving momentum bins and $am_\nu = \frac{m_\nu \cdot c_{ok}^2}{T_{\text{CMB}}}$ the neutrino mass in units of neutrino temperature. Furthermore
$w = \frac{q^3}{1+e^{-q} q^{-\alpha}}$, with $\alpha = 1$.
The third term corresponds to the dark energy content of the universe and ρ_Q is known to be Eq.2.12.

$$\rho_Q = a^{-3(1+w_0+w_a)} e^{3(a-1)w_a} \tag{2.12}$$

The last term in the Eq.2.6 accounts for the curvature of the universe. However, since the universe is assumed to be flat, $\Omega_K = 0$ and this term vanishes.
The dark energy density parameter is given as $\Omega_{\text{DE}} = 1 - \Omega_K - \Omega_r - \Omega_\gamma - \Omega_m$, with the radiation energy density parameter $\Omega_r = (N_{\text{eff}} + N_{m_\nu} e^{\rho_\nu}) \frac{\bar{\rho}_r}{\bar{\rho}_m}$ and the photon energy density parameter $\Omega_\gamma = \frac{\bar{\rho}_\gamma}{\bar{\rho}_m}$. All parameters such as Ω_m, H_0, T_{CMB}, m_ν, N_{eff}, w_0 and w_a can be taken from Tab.2.1. The number of massive neutrino species is set to $N_{m_\nu} = 1$ and the conversion constant is $c_{\text{ok}}^2 = 1.62581581 \cdot 10^{-4}$K/eV.

2.2 Recombination

In the early stages of the universe, baryons and photons were tightly coupled within a hot, dense primordial plasma. At this time, the universe was fully ionized and neutral atoms could not form as any bound state was immediately broken off again by highly energetic photons continuously scattering off free electrons through Eq. 2.13 [5].

$$e^- + \gamma \leftrightarrow e^- + \gamma \tag{2.13}$$

However, as the universe began to expand and cool, its temperature dropped to approximately 3000 K, falling below the binding energy of hydrogen [15].
At this point in time, most protons and electrons combined and formed neutral hydrogen atoms through Eq.2.14. This process is known as recombination [5].

$$e^- + p^+ \rightarrow H + \gamma \tag{2.14}$$

This resulted in the number density of free electrons decreasing significantly, reducing the scattering of photons, which led to the photons decoupling from the primordial plasma and starting to free-stream through the universe. That resulted in the universe becoming fully transparent and the CMB radiation being released. This whole process took place between 290000 and 370000 years after the Big Bang and is sometimes also referred to as last scattering [15].

2.2.1 Optical Depth

In order to define the exact moment of last scattering, the probability of photon scattering has to be considered, this is done by defining the optical depth [5]. When photons travel through a medium, they can get absorbed by that medium, the intensity at which an observer at a distance r then sees light emitted from a source is know to be Eq. 2.15.

$$I(r) = I_0 e^{-\tau(r)} \tag{2.15}$$

where I_0 is the emitting intensity of the source and $\tau(r)$ is the optical depth. The optical depth essentially describes if the medium through which the light is traveling is optically thick ($\tau >> 1$) or optically thin ($\tau << 1$) [15].
The optical depth as a function of conformal time η is calculated as Eq.2.16.

$$\tau(\eta) = \int_{\eta}^{\eta_0} n_e \sigma_T a d\eta \tag{2.16}$$

Here, n_e is the number density of free electrons, $\sigma_T = 6.652462 \cdot 10^{-29} m^2$ is the Thompson cross section and $\eta_0 = \eta(a = 1)$ the conformal time of today [17].

Free electron fraction and electron number density

The electron number density is calculated from the free electron fraction, which is defined as Eq.2.17.

$$X_e = \frac{n_e}{n_H} = \frac{n_e}{n_b} \tag{2.17}$$

Here the total hydrogen number density n_H is equal to the baryon number density n_b. The baryon density can be calculated as Eq.2.18.

$$n_b = \rho_b / m_{\mathrm{H}} = \frac{\Omega_b \rho_{\mathrm{crit}}}{m_{\mathrm{H}} a^3} \tag{2.18}$$

where $m_{\mathrm{H}} = 1.67 \cdot 10^{-27}\mathrm{kg}$[17].
The evolution of the free electron fraction is calculated using the recombination solver implemented in DISCO-EB [2]. This recombination solver is based on the RECFAST model [18], which uses the Saha equation Eq.2.19 before recombination, where all species are relativistic and in thermal equilibrium with each other.

$$\frac{X_e^2}{1 - X_e} \approx \frac{1}{n_b} \left(\frac{m_e T_b}{2\pi} \right)^{3/2} e^{-\epsilon_0 / T_b} \tag{2.19}$$

where $m_e = 9.11 \cdot 10^{-31}\mathrm{kg}$, T_b is the baryon temperature and $\epsilon_0 = 13.61\mathrm{eV}$ is the ionization energy of hydrogen. [17]
During recombination, the primordial plasma falls out of equilibrium and the more accurate Peebles equation Eq.2.20 is used.

$$\frac{dX_e}{dx} = \frac{C_r(T_b)}{H} \left[\beta(T_b)(1 - X_e) - n_H \alpha^2(T_b) X_e^2 \right] \tag{2.20}$$

where the recombination coefficient $C_r(T_b)$ is given by:

$$C_r(T_b) = \frac{\Lambda_{2s\to 1s} + \Lambda_\alpha}{\Lambda_{2s\to 1s} + \Lambda_\alpha + \beta^{(2)}(T_b)}$$

with

$$\Lambda_{2s\to 1s} = 8.227\,\mathrm{s}^{-1}, \quad \Lambda_\alpha = H\frac{(3\epsilon_0)^3}{(8\pi)^2 n_{1s}}, \quad n_{1s} \simeq (1-X_e)n_H$$

$$\beta^{(2)}(T_b) = \beta(T_b)\,e^{3\epsilon_0/(4T_b)}, \quad \beta(T_b) = \alpha^{(2)}(T_b)\left(\frac{m_e T_b}{2\pi}\right)^{3/2} e^{-\epsilon_0/T_b}$$

$$\alpha^{(2)}(T_b) = \frac{64\pi}{\sqrt{27\pi}}\frac{\alpha^2}{m_e^2}\sqrt{\frac{\epsilon_0}{T_b}}\,\phi_2(T_b), \quad \phi_2(T_b) \simeq 0.448\ln\left(\frac{\epsilon_0}{T_b}\right)$$

[17]
Furthermore, RECFAST includes HeI and HeII recombination [18].
From this the electron number density in m^{-3} can be computed as Eq.2.21.

$$n_e = X_e n_b = (1-Y_{\mathrm{HE}})\frac{3H_{0SI}^2 X_e \Omega_b}{8\pi G m_H a^3} \tag{2.21}$$

where $(1-Y_{\mathrm{HE}})$ is the contribution from Helium recombination and $H_{0SI} = \frac{100h\cdot 1000}{3.086\cdot 10^{22}}\mathrm{s}^{-1}$

Opacity

The optical depth can be calculated from the opacity, which is defined as Eq.2.22 [17].

$$-\tau'(\eta) = n_e \sigma_T a \tag{2.22}$$

With putting in the expression for the electron number density Eq.2.21 and rearranging gives Eq. 2.23 in m^{-1}.

$$-\tau'(\eta) = \frac{3\sigma_T}{m_H 8\pi G}\frac{a X_e H_0^2 \Omega_b (1-Y_{\mathrm{HE}})}{a^3}\frac{1}{\frac{\mathrm{m}}{\mathrm{Mpc}}} \tag{2.23}$$

In order to be consistent with the remaining code, this has to be converted from SI units to cosmological units, which is done by keeping H_0 in km/s/Mpc and adding a conversion factor from m to Mpc $\frac{\mathrm{m}}{\mathrm{Mpc}} = 3.086\cdot 10^{22}$.
After combining the constants this leads to a final equation Eq.2.24 for the opacity in units of $\frac{1}{\mathrm{Mpc}}$.

$$-\tau'(\eta) = 2.30\cdot 10^{-9}(1-Y_{\mathrm{HE}})\frac{\Omega_b H_0^2 X_e}{a^2} \tag{2.24}$$

From the opacity the first and second derivatives are calculated numerically with respect to the conformal time.
The optical depth is then calculated through Eq.2.25.

$$\tau(\eta) = \int_\eta^{\eta_0} 2.30\cdot 10^{-9}(1-Y_{\mathrm{HE}})\frac{\Omega_b H_0^2 X_e}{a^2}d\eta \tag{2.25}$$

2.2.2 Visibility function

Another important quantity to describe the processes of recombination is the visibility function, which is defined as Eq.2.26.

$$g(\eta) = -\tau' e^{-\tau} \tag{2.26}$$

here $-\tau'$ is once again the opacity and the functional dependence on η is not explicitly written [15]. The visibility function can be interpreted as a probability function since it is normalized as Eq.2.27.

$$\int_0^{\eta_0} g(\eta) d\eta = 1 \tag{2.27}$$

It describes the probability that a photon observed today was last scattered at a certain conformal time η [17]. The visibility function is often referred to as "last scattering surface" due to its sharp peak at recombination where most of the photons scattered last [15].
The first derivative with respect to the conformal time of the visibility function is calculated as Eq.2.28.

$$g'(\eta) = (-\tau'' - \tau'^2)e^{\tau} \tag{2.28}$$

The second derivative is calculated as Eq.2.29.

$$g''(\eta) = (-\tau''' + 3\tau'\tau'' - \tau^3)e^{\tau} \tag{2.29}$$

2.3 Perturbations

The CMB anisotropies are calculated from perturbations, where both the initial conditions and the evolved perturbative quantities have to be considered. These are taken from the output of DISCO-EB [2]. Here δ is referring to the energy density perturbations, θ to the velocity perturbations and σ are the shear perturbations. All of the perturbations are given in Fourier space.

2.3.1 Initial conditions for perturbative quantities

In order to evolve the perturbations of the different perturbative species, one has to start with defining their initial conditions. These equations are once again taken from the DISCO-EB source code [2].
Background densities [2]
Starting with the isentropic initial conditions for the background densities, these are defined as Eq.2.30.

$$\rho_m = \frac{\bar{\rho}_m \Omega_m}{a^3}, \rho_r = \frac{\bar{\rho}_\gamma + \bar{\rho}_r(N_{\text{eff}} + N_{m_\nu} e^{\bar{\rho}_\nu(a)})}{a^4}, \rho_\nu = \frac{\bar{\rho}_r(N_{\text{eff}} + N_{m_\nu} e^{\bar{\rho}_\nu(a)})}{a^4} \tag{2.30}$$

Metric [2]
The initial condition of the the metric is defined through the metric potential $\boldsymbol{\eta}$ through Eq.2.31.

$$\boldsymbol{\eta} = K_{\text{initial}} \left[1 - \frac{(k\eta)^2}{12\left(15 + 4\frac{\rho_\nu}{\rho_r}\right)} \left(5 + 4s_2^2 \frac{\rho_\nu}{\rho_r} - \frac{\left(16\frac{\rho_\nu}{\rho_r}\frac{\rho_\nu}{\rho_r} + 280\frac{\rho_\nu}{\rho_r} + 325\right)}{10\left(2\frac{\rho_\nu}{\rho_r} + 15\right)} \eta\omega_m \right) \right] \tag{2.31}$$

where $K_{\text{initial}} = -1.0$ is the initial spatial curvature perturbation, $s_2^2 = 1.0$ and $\omega_m = a\frac{\rho_m}{\sqrt{\rho_r}}$.
Photons [2]
The initial conditions for the photon perturbations are given as Eq.2.32, Eq.2.33 and Eq.2.34.

$$\delta_\gamma = -\frac{(k\eta)^2}{3}\left(1 - \frac{\omega_m \eta}{5}\right) K_{\text{initial}} s_2^2 \tag{2.32}$$

$$\theta_\gamma = -\frac{(k\eta)^3}{36\eta}\left[1 - \frac{3}{20\left(1 - \frac{\rho_\nu}{\rho_r}\right)}\left(1 + 5\frac{\Omega_b}{\Omega_m} - \frac{\rho_\nu}{\rho_r}\right)\omega_m\eta\right] K_{\text{initial}} s_2^2 \tag{2.33}$$

$$\sigma_\gamma = 0 \tag{2.34}$$

These are directly connected to the initial conditions of the other components in the following ways:
Baryons [2]

$$\delta_b = 0.75\delta_\gamma, \theta_b = \theta_\gamma \tag{2.35}$$

Cold Dark Matter [2]

$$\delta_c = 0.75\delta_\gamma, \theta_c = 0.0 \tag{2.36}$$

Massless Neutinos [2]

$$\delta_r = \delta_\gamma \tag{2.37}$$

$$\theta_r = -\frac{(k\eta)^4}{36\eta\left(4\frac{\rho_\nu}{\rho_r} + 15\right)}\left[4\frac{\rho_\nu}{\rho_r} + 11 + 12 - \frac{3}{20\left(2\frac{\rho_\nu}{\rho_r} + 15\tau\omega_m\right)}\left(8\frac{\rho_\nu}{\rho_r}\frac{\rho_\nu}{\rho_r} + 50\frac{\rho_\nu}{\rho_r} + 275\right)\right] K_{\text{initial}} \tag{2.38}$$

$$\sigma_r = \frac{(k\eta)^2}{45 + 12\frac{\rho_\nu}{\rho_r}}(3s_2^2 + 1)\left[1 + \frac{\left(4\frac{\rho_\nu}{\rho_r} - 5\right)}{4\left(2\frac{\rho_\nu}{\rho_r} + 15\right)}\eta\omega_m\right] + K_{\text{initial}} \tag{2.39}$$

Massive Neutrinos [2]

$$\delta_\nu = \delta_r, \theta_\nu = \theta_r, \sigma_\nu = \sigma_r \tag{2.40}$$

Dark Energy (Quintessence) [19]

$$\delta_q = \frac{(k\eta)^2}{4} \frac{(1+w_{DE})(4-3c_{s_Q}^2)}{(4-6w+3c_{s_Q}^2)} K_{\textbf{initial}} s_2^2 \tag{2.41}$$

$$\theta_q = \frac{(k\eta)^4}{\eta} \frac{c_{s_Q}^2}{4-6w+3c_{sQ}^2} K_{\text{initial}} s_2^2 \tag{2.42}$$

Here $c_{sQ}^2 = w - \frac{w}{3\mathcal{H}(1+w)}$ is the sound speed of the dark energy perturbation, where w is the equation of state parameter for Dark Energy.
The initial conditions for the perturbations are stored in a perturbation vector Y in DISCO-EB.

2.3.2 Evolution of perturbations

The initial conditions of the perturbations are then evolved through the Einstein-Boltzmann equations. The evolution of the metric perturbations is governed by the Einstein equations, while the individual perturbative species are evolved through the Boltzmann equation [3].

Metric perturbations

The evaluated metric perturbations are taken directly from the source code of DISCO-EB [2] and are defined as Eq.2.43, Eq.2.44, Eq.2.45 and Eq.2.46.

$$\delta\rho = \frac{\bar{\rho}_m(\Omega_c\delta_c + \Omega_b\delta_b)}{a} + \frac{(\bar{\rho}_\gamma\delta_\gamma + \bar{\rho}_r(N_{\text{eff}}\delta_r + N_{m\nu}\delta\rho_\nu)}{a^2} + \bar{\rho}_m\Omega_{\text{DE}}\delta_q\rho_Q a^2 \tag{2.43}$$

$$\delta p = \frac{\bar{\rho}_\gamma\delta_\gamma + \bar{\rho}_r N_{\text{eff}}\delta_r}{3a^2} + \frac{\bar{\rho}_r N_{m_\nu}\delta p_\nu}{a^2} + \left[c_{sQ}^2\bar{\rho}_m\Omega_{DE}\delta_q\rho_Q a^2 + (c_{s_Q}^2 - c_a^2)\frac{3\mathcal{H}(\rho_Q + p_Q)\theta_Q}{k^2}\right] \tag{2.44}$$

$$\delta\theta = \frac{\bar{\rho}_m\left(\Omega_c\theta_c + \Omega_b\theta_b\right)}{a} + \frac{(\Omega_c\theta_c + \Omega_b\theta_b)}{a^2} + \frac{N_{m_\nu}\bar{\rho}_r k f_\nu}{a^2} + (\rho_Q + p_Q)\theta_Q \tag{2.45}$$

$$\delta\sigma = \frac{4\left(\bar{\rho}_\gamma\sigma_\gamma + N_{\text{eff}}\bar{\rho}_r\sigma_r\right)}{3a^2} + \frac{N_{m_\nu}\bar{\rho}_r\sigma_\nu}{a^2} \tag{2.46}$$

Here $\Omega_c = \Omega_m - \Omega_b$ and c_a^2 is the constant adiabatic sound speed of the dark energy perturbation, which can be taken from Tab. 2.1.
The metric perturbations for massive neutrinos are given as Eq.2.50 [2].

$$\delta\rho_\nu = \sum \frac{w\psi_0}{v} \tag{2.47}$$

$$\delta p_\nu = \sum \frac{w\psi_0 v}{3} \tag{2.48}$$

$$f_\nu = \sum w\psi_1 \tag{2.49}$$

$$\sigma_\nu = \frac{2}{3}\sum w\psi_2 v \tag{2.50}$$

The scalar metric potentials are then given as Eq.2.51.

$$\boldsymbol{h}' = \frac{2k^2\boldsymbol{\eta} + \delta\rho}{\mathcal{H}} \text{and } \boldsymbol{\eta}' = \frac{\delta\theta}{2k^2} \tag{2.51}$$

Photon perturbations

The equations of motion of the photon perturbations are defined by a Boltzmann hierarchy of moments, where the first three moments correspond to the density Eq. 2.52, velocity Eq.2.53 and shear Eq.2.54 perturbation [3] and [13].

$$\delta_\gamma = -\frac{4}{3}\theta_\gamma - \frac{2}{3}\boldsymbol{h}' \tag{2.52}$$

$$\theta'_\gamma = k^2\left(\frac{1}{4}\delta_\gamma - \sigma_\gamma\right) - \tau'(\theta_b - \theta_\gamma) \tag{2.53}$$

$$2\sigma'_\gamma = F_\gamma^{(2)\prime} = \frac{8}{15}\theta_\gamma - \frac{3}{15}kF_\gamma^{(3)\prime} + \frac{4}{15}h' + \frac{8}{5}\eta' + \frac{9}{5}\tau'\sigma_\gamma - \frac{1}{10}\tau'\left(G_\gamma^{(0)} + G_\gamma^{(2)}\right) \tag{2.54}$$

The evolution of the higher Boltzmann moments are then given as Eq.2.55 [13].

$$F_\gamma^{(l)\prime} = \frac{k}{2l+1}\left[lF_\gamma^{(l-1)} - (l+1)F_\gamma^{(l+1)}\right] + \tau' F_\gamma^{(l)} \tag{2.55}$$

And the evolution of the polarization moments are defined as Eq.2.56 [13].

$$G_\gamma^{(l)\prime} = \frac{k}{2l+1}\left[lG_\gamma^{l-1} - (l+1)G_\gamma^{(l+1)}\right] - \tau'\left[-G_\gamma^{(l)} + \frac{1}{2}\left(F_\gamma^{(2)} + G_\gamma^{(0)} + G_\gamma^{(2)}\right)\left(\delta_{l0} + \frac{1}{5}\delta_{l2}\right)\right] \tag{2.56}$$

Here δ_{l0} and δ_{l2} are Kronecker symbols. The polarization moments are zero at initial time.

Baryon perturbations

The equations of motion for the baryon perturbations are defined as Eq.2.57 and Eq.2.58 [13].

$$\delta'_b = -\theta_b - \frac{\boldsymbol{h}'}{2} \tag{2.57}$$

$$\theta'_b = -\mathcal{H}\theta_b + c_s^2 k^2 \delta_b - \frac{4}{3}\frac{\bar{\rho}_\gamma}{\bar{\rho}_b}\tau'\sigma_T(\theta_\gamma - \theta_b) \tag{2.58}$$

where the sound speed is Eq.2.59

$$c_s^2 = \frac{1}{3}\frac{k_B\mu T_m\left(4 - \frac{1}{T_m}\frac{d(aTM)}{da}\right)}{m_H c^2} \tag{2.59}$$

with the Boltzmann constant $k_B = 1.381 \cdot 10^{-23}$J/K the speed of light $c = 2.998$m/s, T_m being the temperature and $\frac{d(aTM)}{da}$ is the evolution of temperature with scale factor a and is calculated through the RECFAST class of DISCO-EB.

Cold Dark Matter Perturbations

The equations of state for collisionless cold dark matter are given as Eq.2.60 and Eq.2.61 [13].

$$\delta_c' = -\frac{\boldsymbol{h}'}{2} \tag{2.60}$$

$$\theta_c' = \sigma_c' = 0 \tag{2.61}$$

Dark energy/Quintessence Perturbations

The equations of motions for the dark energy perturbations are defined as Eq.2.62 and Eq.2.63[13].

$$\delta_Q' = -(1+w)\left(\theta_Q + \frac{1}{2}\boldsymbol{h}'\right) - 3\mathcal{H}\left(c_a^2 - w\right)\delta_Q - 9\mathcal{H}(1+w)\left(c_a^2 - c_w^2\right)\frac{\theta_Q}{k^2} \tag{2.62}$$

$$\theta_Q' = -\mathcal{H}(1-3c_a^2)\theta_Q + \frac{c_a^2}{1+w}k^2\delta_Q \tag{2.63}$$

Here $c_w^2 = \mathcal{H}\frac{w-w'}{3(1+w)+10^{-6}}$ is the time derivative of the dark energy sound speed c_{sQ}^2, where $w' = -w_a\mathcal{H}a$ is the time derivative of the equation of state dark energy parameter.

Massless neutrino perturbations

The equations of motions for the massless neutrinos are also defined by a Boltzmann hierarchy of motions, where the first three correspond to the density Eq. 2.64, velocity Eq. 2.65 and shear Eq. 2.66 perturbations [3] and [13].

$$\delta_r' = -\frac{4}{3}\theta_r - \frac{2}{3}\boldsymbol{h}' \tag{2.64}$$

$$\theta_\nu' = k^2\left(\frac{1}{4}\delta_r - \sigma_r\right) \tag{2.65}$$

$$2\sigma_r' = F_r^{(2)'} = \frac{8}{15}\theta_r - \frac{3}{5}kF_r^{(3)} + \frac{4}{15}\boldsymbol{h}' + \frac{8}{5}\boldsymbol{\eta}' \tag{2.66}$$

The higher Boltzmann moments are defined as Eq.2.67 [13].

$$F_r^{(l)'} = \frac{k}{2l+1}\left[lF_r^{(l-1)} - (l-1)F_r^{(l+1)}\right] \tag{2.67}$$

Massive neutrino perturbations

The equation of motions for the massive neutrino perturbations are given by the evolution of a momentum-dependent Boltzmann hierarchy by discretising the momentum space into n bins with momenta q and then evolving the hierarchy for each bin. This leads to the momentum of the neutrino distribution function being defined as Eq.2.68, Eq.2.69 and Eq.2.70 [3].

$$\delta_\nu' = -\frac{qk}{\epsilon}\theta_\nu + \frac{1}{6}h'\frac{d\log f_0}{d\log q} \tag{2.68}$$

$$\theta_\nu' = \frac{qk}{3\epsilon}\left(\delta_\nu - \sigma_\nu\right) \tag{2.69}$$

$$2\sigma_\nu' = \psi_q^{(2)'} = \frac{qk}{5\epsilon}\left(2\theta_\nu - 3\psi_q^{(3)'}\right) - \left(\frac{1}{15}\boldsymbol{h}' + \frac{2}{5}\boldsymbol{\eta}'\right)\frac{d\log f_0}{d\log q} \tag{2.70}$$

Here $\frac{d\log f_0}{d\log q} = -\frac{q}{1+e^{-q}}$ is the derivative of the Fermi-Dirac distribution with $\epsilon = q^2 + (am_\nu)^2$ The higher order Boltzmann moments are defined as Eq.2.71.

$$\psi_q^{(l)'} = \frac{qk}{(2l+1)\epsilon}(l\psi_q^{(l-1)} - (l+1)\psi_q^{l+1}) \tag{2.71}$$

2.4 Line-of-Sight integral

To compute the CMB power spectrum, the photon temperature perturbations have to be expanded in multipoles and then integrated for all l up to which the CMB power spectrum is chosen to be computed. This is computationally very expensive, however, through a technique called line of sight integral the computational effort can be reduced significantly [15]. This method was first introduced in 1996 by Seljak and Zaldarriaga [20]. In order to perform the line-of-sight integration, the equation of photon temperature perturbation first has to be integrated formally and then only after that expanded in multipoles [17]. What this essentially does is to integrate over the physical sources giving rise to the anisotropies in the CMB temperature along the photon past line cone, meaning the line of sight, hence the name. The integral itself then effectively projects the sources onto the 2D sky [20].
To get from the photon perturbation equation to the final expression for the line-of-sight integral, the first step is to write the equation in terms of the conformal time η to get Eq.2.72.

$$\frac{\partial(\Theta+\Psi)}{\partial\eta} + \left(ik\mu - \frac{d\tau}{d\eta}\right)(\Theta+\Psi) + \frac{\partial(\Phi-\Psi)}{\partial\eta} = -\frac{d\tau}{d\eta}\left[\Theta_0 + \Psi + \frac{\Pi}{4} + i\mu v_b - \frac{3\mu^2}{4}\Pi\right] \tag{2.72}$$

After introducing an integrating factor $e^{ik\mu(\eta-\eta_0)-\tau}$ and rearranging, this becomes Eq.2.74.

$$\frac{\partial(\Theta+\Psi)e^{ik\mu(\eta-\eta_0)-\tau}}{\partial\eta} = \frac{\partial(\Psi-\Phi)}{\partial\eta}e^{ik\mu(\eta-\eta_0)}e^{-\tau} \tag{2.73}$$

$$-\frac{d\tau}{d\eta}e^{ik\mu(\eta-\eta_0)}e^{-\tau}\left[\Theta_0+\Psi+\frac{\Pi}{4}\right] - \frac{d\tau}{d\eta}e^{ik\mu(\eta-\eta_0)}e^{-\tau}i\mu v_b + \frac{d\tau}{d\eta}e^{ik\mu(\eta-\eta_0)}e^{-\tau}\frac{3\mu^2}{4}\Pi \tag{2.74}$$

Recognizing $g = -\frac{d\tau}{d\eta}e^{-\tau}$ as the visibility function leads to Eq.2.76.

$$\frac{\partial(\Theta+\Psi)e^{ik\mu(\eta-\eta_0)-\tau}}{\partial\eta} = \frac{\partial(\Psi-\Phi)}{\partial\eta}e^{ik\mu(\eta-\eta_0)}e^{-\tau} \tag{2.75}$$

$$+ge^{ik\mu(\eta-\eta_0)}\left[\Theta_0+\Psi+\frac{\Pi}{4}\right] + ge^{ik\mu(\eta-\eta_0)}i\mu v_b - e^{ik\mu(\eta-\eta_0)}\frac{3\mu^2}{4}g\Pi \tag{2.76}$$

The next step is to integrate the equation over conformal time from the early universe until today which leads to Eq.2.80.

$$(\Theta+\Psi)_{\text{today}} - (\Theta+\Psi)_{\text{ini}}e^{ik\mu(\eta_{\text{ini}}-\eta_0)}e^{-\tau_{ini}} = \int_{\eta_{\text{ini}}}^{\eta_0} d\eta g e^{ik\mu(\eta-\eta_0)}\left[\Theta_0+\Psi+\frac{\Pi}{4}\right] + \tag{2.77}$$

$$\int_{\eta_{\text{ini}}}^{\eta_0} d\eta\frac{\partial(\Psi-\Phi)}{\partial\eta}e^{ik\mu(\eta-\eta_0)}e^{-\tau} + \int_{\eta_{\text{ini}}}^{\eta_0} d\eta g e^{ik\mu(\eta-\eta_0)}i\mu v_b - \int_{\eta_{\text{ini}}}^{\eta_0} d\eta e^{ik\mu(\eta-\eta_0)}\frac{3\mu^2}{4}g\Pi \tag{2.78}$$

The next steps include recognizing that the optical depth τ is huge in the early universe which leads to the convenient approximation of $e^{-\tau_{\text{ini}}} \approx 0$, replacing μ with $-\frac{1}{ik}\frac{d}{d\eta}$, $(ik\mu)^n e^{ik\mu(\eta-\eta_0)} = \frac{d^n}{d\eta^n}e^{ik\mu(\eta-\eta_0})$ and integrating the two last terms by parts, which leads to Eq.2.80.

$$(\Theta+\Psi)_{\text{today}} = \int_{\eta_{\text{ini}}}^{\eta_0} d\eta g e^{ik\mu(\eta-\eta_0)}\left[\Theta_0+\Psi+\frac{\Pi}{4}\right] + \int_{\eta_{\text{ini}}}^{\eta_0} d\eta\frac{\partial(\Psi-\Phi)}{\partial\eta}e^{ik\mu(\eta-\eta_0)}e^{-\tau} \tag{2.79}$$

$$-\int_{\eta_{\text{ini}}}^{\eta_0} d\eta e^{ik\mu(\eta-\eta_0)}\frac{1}{k}\frac{d}{d\eta}(gv_b) + \int_{\eta_{\text{ini}}}^{\eta_0} d\eta e^{ik\mu(\eta-\eta_0)}\frac{3}{4k^2}\frac{d^2}{d\eta^2}g\Pi \tag{2.80}$$

To take multipoles of this expression, the equation has to be multiplied by the Legendre polynomials $\frac{i^l}{2}P_l(\mu)$ and μ has to be integrated over $[-1,1]$, which gives an end result for the line-of-sight integral Eq. 2.81.

$$\Theta_l^{\text{today}}(k) = \int_{\eta_{\text{ini}}}^{\eta_0} d\eta\left[g\left[\Theta_0+\Psi+\frac{\Pi}{4}\right] + \frac{\partial(\Psi-\Phi)}{\partial\eta}e^{-\tau} - \frac{1}{k}\frac{d}{d\eta}(gv_b) + \frac{3}{4k^2}\frac{d^2}{d\eta^2}(g\Pi)\right]j_l(k(\eta_0-\eta)) \tag{2.81}$$

Here $j_l(k(\eta_0-\eta)) = \frac{i^l}{2}\int_{-1}^{1}P_l(k(\eta_0-\eta))e^{-ik(\eta_0-\eta)\mu}d\mu$ are the spherical Bessel functions. This derivation was taken from [15].

2.4.1 Source function

The expression in the brackets of Eq.2.81 can now be defined as the so called "Source function" (Eq.2.82) containing all the physical sources that contribute to the CMB temperature anisotropies.

$$S(k,\eta) = g\left[\Theta_0 + \Psi + \frac{\Pi}{4}\right] + \frac{\partial(\Psi - \Phi)}{\partial\eta}e^{-\tau} - \frac{1}{k}\frac{d}{d\eta}(gv_b) + \frac{3}{4k^2}\frac{d^2}{d\eta^2}(g\Pi) \tag{2.82}$$

Here Ψ and Φ are the metric potentials of the conformal newtonian gauge, v_b is the velocity of the baryon-photon fluid and Π is a polarization term. After taking the derivatives, this gives Eq.2.83.

$$S(k,\eta) = g\left[\Theta_0 + \Psi + \frac{\Pi}{4}\right] + (\Psi' - \Phi')e^{-\tau} - \frac{1}{k}(g'v_b + v_b g') + \frac{3}{4k^2}(g''\Pi + 2g'\Pi' + \Pi'' g) \tag{2.83}$$

This equation represents the most general form of the source function in the conformal Newtonian gauge.

Gauge Transformation

Since the perturbations used in DISCO-EB are defined in the synchronous gauge, a gauge transformation of the source function has to be performed. To make the source function gauge consistent with the rest of the code, an additional term α Eq.2.84 that drives the transformation, consisting of the metric potentials $\boldsymbol{h}$ and $\boldsymbol{\eta}$ of the synchronous gauge, has to be introduced.

$$\alpha = \frac{\boldsymbol{h}' + \boldsymbol{\eta}'}{2k^2} \tag{2.84}$$

Putting in the expressions for $\boldsymbol{h}'$ and $\boldsymbol{\eta}'$ given in Eq. 2.51 in the equation defining α Eq.2.84 and then taking the derivatives leads to α' Eq.2.85 and α'' Eq.2.86.

$$\alpha' = \frac{\boldsymbol{h}'' + \boldsymbol{\eta}'}{2k^2} = -\frac{3\delta\sigma}{2k^2} + \boldsymbol{\eta} - 2\mathcal{H}\alpha \tag{2.85}$$

$$\alpha'' = \frac{\boldsymbol{h}''' + \boldsymbol{\eta}'''}{2k^2} = -\frac{3\delta\sigma'}{2k^2} + \boldsymbol{\eta}' - 2\mathcal{H}'\alpha - 2\mathcal{H}\alpha' \tag{2.86}$$

Here $\delta\sigma'$ is calculated from Eq.2.46 to be Eq.2.87.

$$\delta\sigma' = \frac{4\left(\bar{\rho}_\gamma\sigma'_\gamma + N_{\mathrm{eff}}\bar{\rho}_r\sigma'_r\right)}{3a^2} + \frac{N_{m_\nu}\bar{\rho}_r\sigma'_\nu}{a^2} - 2\mathcal{H}\delta\sigma \tag{2.87}$$

Furthermore $\mathcal{H}'$ is calculated from Eq.2.5 as Eq.2.88.

$$\mathcal{H}' = \frac{\bar{\rho}'}{2\sqrt{3\bar{\rho}}} \tag{2.88}$$

where $\bar{\rho}'$ is the derivative of the background density Eq.2.89.

$$\bar{\rho}' = -\frac{\bar{\rho}_m \Omega_m}{a} - 2\frac{(\bar{\rho}_\gamma + \bar{\rho}_r)(N_{\text{eff}} + N_{m\nu}\bar{\rho}_\nu)}{a^2} + \frac{\bar{\rho}_m \Omega_{\text{DE}}(-3(1 + w_a \rho_Q a^2 + 2\rho_Q a^2)\mathcal{H}\bar{\rho}_r N_{m_\nu}\rho'_\nu}{a^2} \tag{2.89}$$

Here ρ'_ν is the derivative of the massive neutrino energy density given by Eq.2.90.

$$\rho'_\nu = \sum w \frac{v^2 \psi^{(0)\prime}}{v - \psi^{(0)}} v' \tag{2.90}$$

In this expression $v' = \left(\frac{aq \cdot aq'}{(1+aq^2)}\right)^2$ is the comvoing momentum of the neutrino, where $aq' = \mathcal{H} \cdot aq$. These are taken from the DISCO-EB source code [2].
The transformation from the conformal Newtonian gauge to the synchronous gauge is then governed by the following set of equations given in Eq. 2.94 [13].

$$\delta(\text{Syn}) = \delta(\text{Con}) - \alpha \frac{\bar{\rho}'}{\bar{\rho}} \tag{2.91}$$

$$\theta(\text{Syn}) = \theta(\text{Con}) - \alpha k^2 \tag{2.92}$$

$$\delta P(\text{Syn}) = \delta P(\text{Con}) - \alpha \bar{P}' \tag{2.93}$$

$$\sigma(\text{Syn}) = \sigma(\text{Con}) \tag{2.94}$$

Furthermore, Eq.2.83 can be decomposed into four distinct terms, each corresponding to a different physical effect.

Sachs-Wolfe effect

The first term to consider gives rise to the Sachs-Wolfe effect, this includes all the quantities that are multiplied with the visibility function g, meaning Eq.2.95.

$$S_1(k, \eta) = g \left[\Theta_0 + \Psi + \frac{1}{4}\Pi - \frac{1}{k}v'_b + \frac{3}{4k^2}\Pi''\right] \tag{2.95}$$

The Sachs-Wolfe term accounts for both the intrinsic photon density fluctuations, given by the monopole term $\Theta_0 = \frac{1}{4}\delta_\gamma$ and the gravitational redshift experienced by photons as they climb out of potential wells, described by the metric perturbation Ψ. Here $\Psi < 0$ leads to an over-dense region, where photons lose energy climbing out, leading to a redshift and a cold spot observed in the CMB. Conversely $\Psi > 0$ leads to an under-dense region, producing a hot spot due to the blue-shift of photons [5].
The first quantity to investigate is $\Theta_0 = \frac{1}{4}\delta_\gamma$, which needs to be gauge transformed using Eq.2.94. The starting point for this is Eq.2.96.

$$\frac{1}{4}\delta_\gamma(\text{Con}) = \frac{1}{4}\delta_\gamma(\text{Syn}) + \alpha \frac{\bar{\rho}'}{\bar{\rho}} \tag{2.96}$$

Here $\frac{\bar{\rho}'}{\bar{\rho}}$ can be calculated through using the continuity equation Eq.2.97.

$$\bar{\rho}' + 3\mathcal{H}(\bar{\rho} + \bar{P}) = 0 \tag{2.97}$$

Using the equation of state parameter $w = \frac{p}{\rho}$ the continuity equation becomes Eq.2.98.

$$\bar{\rho}' + 3\mathcal{H}\bar{\rho}(1+w) = 0 \tag{2.98}$$

Since this corresponds to the photon perturbations, the value for the equation of state parameter $w = 1/3$ for radiation is chosen. Putting $\bar{\rho}'$ to the other side and dividing by $\bar{\rho}$ then leads to Eq.2.99.

$$\frac{\bar{\rho}'}{\bar{\rho}} = -4\mathcal{H} \tag{2.99}$$

With that the final gauge consistent expression for the photon monopole is Eq.2.100.

$$\Theta_0 = \frac{1}{4}\delta_\gamma(\mathrm{Syn}) - \mathcal{H}\alpha \tag{2.100}$$

The next quantity to be investigated is the conformal metric potential Ψ, which in the synchronous gauge can be expressed by $\boldsymbol{h}$ and $\boldsymbol{\eta}$ and their derivatives through Eq.2.101 [13].

$$\Psi = \frac{1}{2k^2}(\boldsymbol{h}'' + 6\boldsymbol{\eta}'' + \mathcal{H}(\boldsymbol{h}' + 6\boldsymbol{\eta}')) \tag{2.101}$$

With remembering the expression α Eq.2.84 and the derivative Eq.2.85, this can be expressed as Eq.2.102.

$$\Psi = \alpha' + \mathcal{H}\alpha \tag{2.102}$$

The next quantity to have a closer look at is the polarization term $\frac{1}{4}\Pi$ which is defined as Eq.2.104 [17].

$$\frac{1}{4}\Pi = \frac{1}{4}\left(\Theta_2 + \Theta_P^{(0)} + \Theta_P^{(2)}\right) \tag{2.103}$$

with $\Theta_2 = \frac{1}{4}F_\gamma^{(2)}$, $\Theta_P^{(0)} = \frac{1}{4}G_\gamma^{(0)}$ and $\Theta_P^{(2)} = \frac{1}{4}G_\gamma^{(2)}$, this becomes Eq.2.104.

$$\frac{1}{4}\Pi = \frac{1}{16}\left(F_\gamma^{(2)} + G_\gamma^{(0)} + G_\gamma^{(2)}\right) \tag{2.104}$$

Here $F_\gamma^{(2)} = 2\sigma_\gamma$ and $G_\gamma^{(0)}$ and $G_\gamma^{(2)}$ are the first and third polarization moment.
The next term to have a closer look at is $-\frac{1}{k}v_b'$, where v_b can be expressed through the velocity perturbation θ_b as Eq.2.105.

$$v_b = -\frac{1}{k}\theta_b \tag{2.105}$$

This leads to Eq.2.106

$$-\frac{1}{k}v_b' = \frac{1}{k^2}\theta_b' \tag{2.106}$$

This expression has to be gauge transformed with Eq.2.94, the starting point for this is Eq.2.107.

$$\theta_b(\mathrm{Con}) = \theta_b(\mathrm{Syn}) + \alpha k^2 \tag{2.107}$$

After taking the derivative and putting it back into Eq.2.106 this gives Eq.2.108

$$\frac{1}{k^2}\theta_b' = \frac{1}{k^2}\theta_b' + \alpha' \tag{2.108}$$

For the next term $\frac{3}{4k^2}\Pi''$, the derivatives of the polarization term Π have to be computed. The starting point for the first derivative Π' is Eq.2.109.

$$\Pi' = \frac{1}{4}\left(F_\gamma^{(2)'} + G_\gamma^{(0)'} + G_\gamma^{(2)'}\right) \tag{2.109}$$

For the individual derivatives of the moments Eq.2.55 and Eq.2.56 are used. These derivatives could also be directly called from DISCO-EB, however, calculating them by hand will prove useful for calculating Π''.
For $F_\gamma^{(2)'}$ this leads to Eq.2.110.

$$F_\gamma^{(2)'} = \frac{k}{5}\left(2F_\gamma^{(1)} - 3F_\gamma^{(3)}\right) + \tau' F_\gamma^{(2)} \tag{2.110}$$

using $\theta_\gamma = \frac{3}{4}kF_\gamma^{(1)}$ and performing the gauge transformation $\theta_\gamma(\text{Con}) = \theta_\gamma(\text{Syn}) + \alpha k^2$ this can be expressed as Eq.2.111.

$$F_\gamma^{(2)'} = \frac{8}{15}(\theta_\gamma + \alpha k^2) - \frac{3k}{5}F_\gamma^{(3)} + \tau' F_\gamma^{(2)} \tag{2.111}$$

The higher Boltzmann moments are gauge invariant and therefore don't need to be transformed.
The derivative of $G_\gamma^{(0)}$ is calculated as Eq.2.112.

$$G_\gamma^{(0)'} = -kG_\gamma^{(1)} - \tau'\frac{1}{2}\left(F_\gamma^{(2)} - G_\gamma^{(0)} + G_\gamma^{(2)}\right) \tag{2.112}$$

Furthermore, $G_\gamma^{(2)'}$ is calculated as Eq.2.113

$$G_\gamma^{(2)'} = \frac{k}{5}\left(2G_\gamma^{(1)} - 3G_\gamma^{(3)}\right) - \tau'\left[\frac{1}{10}\left(F_\gamma^{(2)} + G_\gamma^{(0)}\right) - \frac{9}{10}G_\gamma^{(2)}\right] \tag{2.113}$$

Putting these together then gives Eq.2.114.

$$\Pi' = \frac{1}{4}\left[\frac{8}{15}(\theta_\gamma + \alpha k^2) - \frac{3k}{5}F_\gamma^{(3)} - \frac{3k}{5}G_\gamma^{(3)} + \frac{4}{10}\tau' F_\gamma^{(2)} - \frac{3k}{5}G_\gamma^{(1)} + \frac{4}{10}\tau' G_\gamma^{(0)} + \frac{4}{10}\tau' G_\gamma^{(2)}\right] \tag{2.114}$$

This can be simplified further as Eq.2.115.

$$\Pi' = \frac{1}{4}\left[\frac{8}{15}(\theta_\gamma + \alpha k^2) - \frac{3k}{5}\left(F_\gamma^{(3)} + G_\gamma^{(1)} + G_\gamma^{(3)}\right) + \frac{4}{10}\tau'\Pi\right] \tag{2.115}$$

The second derivative of Π can then be expressed as Eq. 2.116.

$$\Pi'' = \frac{1}{4}\left[\frac{8}{15}(\theta_\gamma' + \alpha' k^2) - \frac{3k}{5}\left(F_\gamma^{(3')} + G_\gamma^{(1')} + G_\gamma^{(3')}\right) + \frac{4}{10}\tau''\Pi + \frac{4}{10}\tau'\Pi'\right] \tag{2.116}$$

Here all of the individual derivatives can either be directly taken from the DISCO-EB output or have already been calculated prior to this.
With that the last part of the Sachs-Wolfe Term becomes Eq.2.117.

$$\frac{3}{4k^2}\Pi'' = \frac{3}{16k^2}\left[\frac{8}{15}(\theta'_\gamma + \alpha' k^2) - \frac{3k}{5}\left(F_\gamma^{(3')} + G_\gamma^{(1')} + G_\gamma^{(3')}\right) + \frac{4}{10}\tau''\Pi + \frac{4}{10}\tau'\Pi'\right] \tag{2.117}$$

With putting everything back together, the final Sachs-Wolfe Term of the Source Function is Eq.2.118 with Π and Π'' as Eq.2.104 and Eq. 2.116 respectively.

$$S_1(k,\eta) = g\left[\frac{1}{4}\delta_\gamma + 2\alpha' + \frac{1}{16}\Pi + \frac{1}{k^2}\theta'_b + \frac{3}{4k^2}\Pi''\right] \tag{2.118}$$

Integrated Sachs-Wolfe effect

The next term to investigate closer gives rise to the Integrated Sachs-Wolfe effect, this refers to the following term Eq.2.119.

$$S_2(k,\eta) = e^{-\tau}(\Psi' - \Phi') \tag{2.119}$$

The integrated Sachs-Wolfe corresponds to an additional gravitational redshift that comes from the evolution of metric potentials, hence gravitational fields, along the line-of-sight. This mainly contributes during early times of matter domination, where the remaining amount of radiation lead to the potentials changing with time, and during late times where dark energy starts dominating. During matter domination, the gravitational potentials were constant, leading to no contribution from the Integrated Sachs-Wolfe effect from that epoch [5]. For this term, the derivatives metric potential have to be looked at closer. With Ψ already defined as Eq.2.102, the derivative is calculated as Eq.2.120.

$$\Psi' = \alpha'' + \mathcal{H}'\alpha + \alpha'\mathcal{H} \tag{2.120}$$

The second metric potential Φ is defined as Eq.2.122 [13].

$$\Phi = -\phi = -\boldsymbol{\eta} + \mathcal{H}\alpha \tag{2.121}$$

This leads to the derivative being calculated as Eq.2.122

$$\Phi' = -\boldsymbol{\eta}' + \mathcal{H}'\alpha + \alpha'\mathcal{H} \tag{2.122}$$

After putting these back into the Integrated Sachs-Wolfe term, the final expression is Eq.2.123.

$$S_2(k,\eta) = e^{-\tau}(\alpha'' + \boldsymbol{\eta}') \tag{2.123}$$

Doppler effect

The third term to have a closer look at gives rise to the Doppler effect, this includes all terms that are multiplied with the derivative of the visibility function g' Eq.2.125.

$$S_3(k,\eta) = g'\left(-\frac{1}{k}v_b + 2\frac{3}{4k^2}\Pi'\right) \tag{2.124}$$

The Doppler effect comes from the motion of the baryon-photon fluid. The photons that are moving away from us are red-shifted, while the ones moving towards us are blue-shifted. [5]. Since all of the quantities in this term have already been calculated previously, the final expression of the Doppler term becomes Eq.2.125 where Π' is taken to be Eq. 2.115.

$$S_3(k,\eta) = g'\left(\frac{1}{k^2}\theta_b + \alpha + \frac{2}{3k^2}\Pi'\right) \tag{2.125}$$

Polarization term

The last remaining term is an additional polarization term, which includes the second derivative of the visibility function g''. Eq.2.126.

$$S_4(k,\eta) = g''\frac{3}{4k^2}\Pi \tag{2.126}$$

This term gives rise to the polarization coming from Thompson scattering. All of the included quantities have already been calculated, so the terms stays as is.

Final Source Function

After putting all of the terms together the final expression for the source function then becomes Eq.2.127.

$$S(k,\eta) = g\left(\frac{1}{4}\delta_\gamma + 2\alpha' + \frac{1}{4}\Pi + \frac{1}{k^2}\theta_b' + \frac{3}{4k^2}\Pi''\right) + e^{-\tau}(\alpha'' + \boldsymbol{\eta}') + g'\left(\frac{1}{k^2}\theta_b + \alpha + \frac{3}{2k^2}\Pi'\right) + g''\frac{3}{4k^2}\Pi \tag{2.127}$$

2.4.2 Spherical Bessel functions

For expanding the sources into multipoles, the source function is multiplied with the spherical Bessel functions. The spherical Bessel functions j_l are defined through Eq.2.128.

$$\frac{d^2 j_l}{dx^2} + \frac{2}{x}\frac{dj_l}{dx} + \left(1 - \frac{l(l+1)}{x^2}\right) j_l = 0 \tag{2.128}$$

Here the two lowest order solutions are defined as Eq.2.129 and the higher orders of the functions can be calculated through the recursion relation given in Eq.2.130.

$$j_0(x) = \frac{\sin(x)}{x}, j_1(x) = \frac{\sin(x) - \cos(x)}{x^2} \tag{2.129}$$

$$j_{l+1} = \frac{2l+1}{x} j_l - j_{l-1} \tag{2.130}$$

The argument for which the spherical Bessel are calculated in this case is $x = k(\eta_0 - \eta)$ [5].

2.5 CMB power spectrum

The CMB anisotropy power spectrum observed today can be approximated by evaluating the two-point angular correlation function $C_l \approx \Theta_l^2(\vec{x})$ at the origin $\vec{x} = 0$. To obtain this, the computed multipole moments $\Theta_l^2(k)$ must be Fourier transformed and additionally, to account for the scale dependence of the initial perturbations, the result must be weighted by the primordial power spectrum $\mathcal{P}_R(k)$ [17]. This yields to the final expression for C_l as given in Eq.2.131.

$$C_l = 4\pi \int d\ln k \Theta_l^2(k) \Delta_R^2(k) \tag{2.131}$$

Here $\Delta_R^2(k) = \frac{k^3}{2\pi^2} \mathcal{P}_R(k)$ with the primordial power spectrum being Eq.2.132.

$$\mathcal{P}_R(k) = A_s \left(\frac{k}{k_{\text{piviot}}} \right)^{n_s - 1} \tag{2.132}$$

where A_s is the amplitude of the scalar curvature perturbations, k_{piviot} is a reference scale and n_s is the spectral index [5]. These constants can be taken from Tab2.1. What is usually plotted as the CMB spectrum is the normalized quantity D_ℓ in units of K^2 this is calculated as Eq.2.133 [5].

$$D_\ell = \frac{\ell(\ell+1)}{2\pi} C_\ell T_0^2 \tag{2.133}$$

2.6 Anisotropy map

The power spectrum quantifies the amount of fluctuation power present at different angular scales on the sky, so essentially, it represents the variance of the CMB temperature fluctuations at each angular scale ℓ. To analyze these anisotropies, the CMB temperature field on the sky is expanded in spherical harmonics as Eq.2.134 [5].

$$\Theta(\hat{\boldsymbol{n}}) = \sum_{l=2}^{\infty} \sum_{m=-l}^{l} a_{\ell m} Y_{\ell m}(\hat{\boldsymbol{n}}) \tag{2.134}$$

The expansion coefficients $a_{\ell m}$ are commonly referred to as spherical harmonics coefficient. To generate a CMB anisotropy map, so essentially a Gaussian realization of the power spectrum, each coefficient a_{lm} is drawn from a Gaussian distribution with zero mean and variance given by the power spectrum $\langle |a_{lm}|^2 \rangle = C_\ell$ as in Eq.2.135.

$$a_{\ell m} \sim \mathcal{N}(0, C_\ell) \tag{2.135}$$

The coefficients a_{lm} must be generated for each combination of ℓ and m while ensuring, that the condition specified in Eq.2.136 is met.

$$a_{l,-m} = (-1)^m a_{lm}^* \tag{2.136}$$

In generate sky maps from the coefficients a_{lm}, an inverse spherical harmonics transformation must be performed, reconstructing the temperature field from the a_{lm} values drawn from the power spectrum as Eq.2.134 [21].

3 Code

3.1 Setting up the background cosmology

The first step is to set up the cosmological background in the code. This begins by storing all the constants listed in Tab.2.1in a structured list. Next, the evolve_background function from DISCO-EB is called. This function computes the full background evolution, providing the expansion history and samples a range of Fourier modes and scale factors. Additionally, the get_perturbations function is called to import all relevant perturbation variables. At this stage the conformal time is also defined, computed from the scale factor. Finally, the code specifies the maximum multipole moment l_{max} at which the Boltzmann hierarchies are truncated for each relevant component. This is done through the code snippet shown in List.3.1.

```
import jax
jax.config.update("jax_enable_x64", True) # unfortunately we currently require double precision
import jax.numpy as jnp
import matplotlib.pyplot as plt
from functools import partial

## these are the main modules for background evolution and perturbation evolution
from discoeb.background import evolve_background
from discoeb.cosmo import get_aprimeoa
from discoeb.perturbations import evolve_perturbations, get_power, model_synchronous, nu_perturb, nu_perturb_prime
from discoeb.spline_interpolation import spline_interpolation
from discoeb.util import spherical_bessel

param = {}
# OmegaDE is inferred since flatness is assumed currently
param['Omegam']  = 0.3099          # Total matter density parameter
param['Omegab']  = 0.0488911       # Baryon density parameter
param['w_DE_0']  = -0.99           # Dark energy equation of state parameter today
param['w_DE_a']  = 0.0             # Dark energy equation of state parameter time derivative
param['cs2_DE']  = 1.0             # Dark energy sound speed squared
param['Omegak']  = 0.0
param['A_s']     = 2.1064e-09      # Scalar amplitude of the primordial power spectrum
param['n_s']     = 0.96822         # Scalar spectral index
param['H0']      = 67.742          # Hubble constant today in units of 100 km/s/Mpc
```

```python
param['Tcmb']    = 2.7255            # CMB temperature today in K
param['YHe']     = 0.248             # Helium mass fraction
param['Neff']    = 2.046             # Effective number of ultrarelativistic neutrinos
                                      # -1 if massive neutrino present
param['Nmnu']    = 1                 # Number of massive neutrinos (must be 1 currently)
param['mnu']     = 0.06              # Sum of neutrino masses in eV
param['k_p']     = 0.05              # Pivot scale in 1/Mpc

# modes to sample
nmodes = 1024                         # number of modes to sample
kmin   = 1e-5                         # minimum k in 1/Mpc
kmax   = 2e-1                         # maximum k in 1/Mpc
aexp   = 1.0                          # scale factor at which to evaluate the power spectrum

## Compute Background+thermal evolution
param = evolve_background(param=param, thermo_module='RECFAST')
# # compute perturbation evolution
aexp_out = jnp.geomspace(3e-4, 5e-3, 300, endpoint=False)
aexp_out = jnp.append( aexp_out, jnp.geomspace(5e-3, 1.0, 64))

# # new option return_full to return the full output
@partial( jax.jit, static_argnames = 'nmodes')
def get_perturbations( param, kmin, kmax, nmodes, aexp_out ):
  y, kmodes, param = evolve_perturbations( param=param, kmin=kmin, kmax=kmax, num_k=nmodes, aexp_out=aexp_out,
                                    # lmaxg = 31, lmaxgp = 31, lmaxr = 31, lmaxnu = 31, nqmax = 5, # from compare_class
                                    rtol=1e-3, atol=1e-3 , return_full=True ,
                                    dologk=False, # put true here to make it go faster
                                    )

  tau = param['tau_out']
  lmaxg = param['lmaxg']
  lmaxgp = param['lmaxgp']
  lmaxr = param['lmaxr']
  lmaxnu = param['lmaxnu']
  nqmax = param['nqmax']
  idxtau = jnp.arange(len(tau))
  idxk = jnp.arange(len(kmodes))
  yprime = jax.vmap( lambda ik : jax.vmap( lambda itau : model_synchronous( tau=tau[itau], y=y[ik,itau,:], param=param, kmode=kmodes[ik], lmaxg=lmaxg, lmaxgp=lmaxgp, lmaxr=lmaxr, lmaxnu=lmaxnu, nqmax=nqmax ) )(idxtau) )(idxk)

  return y, yprime, kmodes, param

yout, youtprime, kmodes, param = get_perturbations( param=param, kmin=kmin, kmax=kmax, nmodes=nmodes, aexp_out=aexp_out )
```

```

tau = param['tau_out']
lmaxg = param['lmaxg']
lmaxgp = param['lmaxgp']
lmaxr = param['lmaxr']
lmaxnu = param['lmaxnu']
nqmax = param['nqmax']
idxtau = jnp.arange(len(tau))
idxk = jnp.arange(len(kmodes))
```

Listing 3.1: Setting up the background and calling the perturbations of DISCOEB

The next step is to define the background density and set up the neutrino momentum grid as illustrated in List.3.2.

```
a = aexp_out
tau = param['tau_of_a_spline'].evaluate(a) # confromal time
Omegac = param['Omegam'] - param['Omegab']
rhonu = jnp.exp(param['logrhonu_of_loga_spline'].evaluate(jnp.log(a)))
rho_Q = a**(-3*(1+param['w_DE_0']+param['w_DE_a'])) * jnp.exp(3*(a-1)*
    param['w_DE_a'])
pnu = jnp.exp(param['logpnu_of_loga_spline'].evaluate( jnp.log(a) ) )
w_Q = param['w_DE_0'] + param['w_DE_a'] * (1.0 - a)
rho_plus_p = rhonu + pnu

grho = (
    param['grhom'] * param['Omegam'] / a
    + (param['grhog'] + param['grhor'] * (param['Neff'] + param['Nmnu'] *
     rhonu)) / a**2
    + param['grhom'] * param['OmegaDE'] * rho_Q * a**2
    + param['grhom'] * param['Omegak']
)
gpres = (
    (param['grhog'] + param['grhor'] * param['Neff']) / 3.0 + param['
    grhor'] * param['Nmnu'] * pnu
) / a**2 + w_Q * param['grhom'] * param['OmegaDE'] * rho_Q * a**2

photbar = param['grhog'] / (param['grhom'] * param['Omegab'] * a)
pb43 = 4.0 / 3.0 * photbar
cs2 = param['cs2a_of_tau_spline'].evaluate( tau ) / a
K = 0
s2_squared = 1.-3.*K/kmodes**2
s_l3 = 1.0
s_l2 = 1.0

# neutrino grid
iq0 = 10 + lmaxg + lmaxgp + lmaxr
iq1 = iq0 + nqmax
iq2 = iq1 + nqmax
iq3 = iq2 + nqmax
iq4 = iq3 + nqmax
ell  = jnp.arange(3, lmaxg )
```

Listing 3.2: Defining the background density and the neutrino grid

3.2 Recombination

Recombination is initialized within the background class of DISCO-EB as shown in List.3.3. This process begins by extracting the free electron fraction x_e from the recombination solver. From x_e all relevant quantities are computed. The opacity is then interpolated using DISCO-EBs spline interpolation class, which constructs a cubic spline over a grid in conformal time. This provides a smooth and efficient representation of the opacity, enabling evaluation at arbitrary conformal times. The optical depth is computed by numerically integrating the interpolated opacity using spline integration. All recombination related parameters are finally stored in the parameter list for later use.

```
# compute optical depth and visibility functions
    akthom = 2.3038921003709498e-9 * (1.0 - param['YHe']) * param['Omegab'] * param['H0']**2
    # grho_v = jax.vmap( lambda a: grho( param, a ) )( a )(aexp)
    # aprimeoa = jnp.sqrt( grho_v / 3.0 )
    aprimeoa = get_aprimeoa( param=param, aexp=aexp )

    tau_pre_recomb = param['tau_of_a_spline'].evaluate( 1e-4 )
    xe_full   = 1 + param['YHe'] / (1 - param['YHe'])
    xe        = jnp.where( tau <= tau_pre_recomb, xe_full, param['xe_of_tau_spline'].evaluate( tau ) )
    xeprime   = jnp.where( tau <= tau_pre_recomb, 0.0, param['xe_of_tau_spline'].derivative( tau ) )

    # xe = param['xe_of_tau_spline'].evaluate( tau )
    # xeprime = param['xe_of_tau_spline'].derivative( tau )
    # xepprime  = param['xe_of_tau_spline'].derivative2( tau )
    opac      = xe * akthom / aexp**2

    opacspline = spline_interpolation( tau, opac, integrate_from_start=False)
    opacprime  = opacspline.derivative( tau )
    opacpprime = opacspline.derivative2( tau )
    # opacprime = xeprime * akthom / aexp**2 - 2 * xe * akthom / aexp**2 * aprimeoa

    optical_depth = opacspline.integral( tau )
    optical_depth_today = opacspline.integral( param['tau_of_a_spline'].evaluate( 1.0 ) )
    optical_depth -= optical_depth_today

    # optical_depth = jnp.array([optical_depth[0], *optical_depth])
    expmmu    = jnp.exp(-optical_depth)
    vis       = opac * expmmu
    dvis      = (opacprime + opac**2) * expmmu
    ddvis     = (opacpprime + 3 * opac * opacprime + opac**3) * expmmu

    param['optical_depth'] = optical_depth
    param['opac'] = opac
    param['gvis'] = vis
    param['gvisprime'] = dvis
```

```
    param['gvispprime'] = ddvis

    if thermo_module == 'RECFAST':
        param['xeprime_recf'] = xeprime_recfast

    param['xeprime'] = xeprime
```

Listing 3.3: Setting up the recombination parameters, meaning the free electron fraction, the opacity, the optical depth and the visibility function and derivatives

Recombination is then called as List.3.4.

```
opacspline = spline_interpolation( jnp.log(param['tau']), param['opac'] )
opac = opacspline.evaluate( jnp.log(tau) )
opacprime = opacspline.derivative( jnp.log(tau) ) / tau # derivative
    after log(tau): more accuracy etc

isub = jnp.logical_and(param['aexp'] > 1.1e-4, param['aexp'] <= 1.0)
tempb = param['tempba_of_tau_spline'].evaluate( jnp.log(tau) )  / a #
    baryon temperture
gvis = spline_interpolation( jnp.log(param['tau'][isub]), param['gvis'][
    isub] ).evaluate( jnp.log(tau) )
gvisprime = spline_interpolation( jnp.log(param['tau'][isub]), param['
    gvisprime'][isub] ).evaluate( jnp.log(tau) )
gvispprime = spline_interpolation( jnp.log(param['tau'][isub]), param['
    gvispprime'][isub] ).evaluate( jnp.log(tau) )
optical_depth = jnp.exp(spline_interpolation( jnp.log(param['tau'][isub])
    , jnp.log(jnp.maximum(param['optical_depth'][isub],1e-10)) ).evaluate(
     jnp.log(tau) ))
```

Listing 3.4: Calling the recombination parameters in a jupyter notebook

3.3 Perturbations

Both the initial conditions and the evolved perturbations are stored in a vector that can be accessed within a Jupyter notebook, as shown in List.3.5. All perturbations are computed in the perturbation class of DISCO-EB.

```
yprime = youtprime
kmode = kmodes[:,None]

idxb  = 5
idxg  = 7
idxgp = 7 + (lmaxg+1)
idxr  = 9 + lmaxg + lmaxgp

# ahprime = yout[...,1]
eta = yout[...,2]

# ... cdm
deltac = yout[...,3]
thetac = yout[...,4]

```

```
# ... baryons
deltab = yout[...,idxb]
thetab = yout[...,idxb+1]

# ... photons
deltag = yout[...,idxg]
thetag = yout[...,idxg+1]
shearg = yout[...,idxg+2] / 2.0

# ... massless neutrinos
deltar = yout[..., idxr]
thetar = yout[..., idxr+1]
shearr = yout[..., idxr+2] / 2.0

# ... quintessence field
deltaq = yout[...,-2]
thetaq = yout[...,-1]

# ... baryons
deltabprime = youtprime[..., idxb]
thetabprime = youtprime[..., idxb+1]

# ... photons
deltagprime = youtprime[..., idxg]
thetagprime = youtprime[..., idxg+1]
sheargprime = youtprime[..., idxg+2] / 2.0

# ... massless neutrinos
deltarprime = youtprime[..., idxr]
thetarprime = youtprime[..., idxr+1]
shearrprime = youtprime[..., idxr+2] / 2.0
```

Listing 3.5: Calling the pertubations from the perturbation vector

In addition, specific components such as dark energy quantities and neutrino perturbations must be explicitly defined. These are computed using individual functions within the perturbation class. Metric perturbations also need to be specified at this stage. This is shown in List.3.6.

```
cs2_Q              = param['cs2_DE']
w_Q                = param['w_DE_0'] + param['w_DE_a'] * (1.0 - a)
rho_Q              = a**(-3*(1+param['w_DE_0']+param['w_DE_a'])) * jnp.
    exp(3*(a-1)*param['w_DE_a'])
rho_plus_p_theta_Q = (1+w_Q) * rho_Q * param['grhom'] * param['OmegaDE']
    * thetaq * a**2

aprimeoa = jax.vmap( lambda ia: get_aprimeoa( param=param, aexp=aexp_out[
    ia] ) )(idxtau)

 # quintessence EOS time derivatives
w_Q_prime = -param['w_DE_a'] * aprimeoa * a
ca2_Q     = w_Q - w_Q_prime / 3 / ((1+w_Q)+1e-6) / aprimeoa

drhonu, dpnu, fnu, shearnu = jax.vmap( lambda ik : jax.vmap( lambda ia :
```

```
    nu_perturb( aexp_out[ia], param[’amnu’], yout[ik,ia,iq0:iq1], yout[ik,ia,iq1:iq2], yout[ik,ia,iq2:iq3], nqmax=nqmax ) )(idxtau) )(idxk)
rho_nu_prime, shear_nu_prime = jax.vmap( lambda ik : jax.vmap( lambda ia : nu_perturb_prime( a=aexp_out[ia], amnu=param[’amnu’], aprimeoa=aprimeoa[ia], psi0=yout[ik,ia,iq0:iq1], psi2=yout[ik,ia,iq2:iq3], psi0prime=yprime[ik,ia,iq0:iq1], psi2prime=yprime[ik,ia,iq2:iq3], nqmax=nqmax ) )(idxtau) )(idxk)
grhoprime = (
    -param[’grhom’] * param[’Omegam’] / a
    -2*(param[’grhog’] + param[’grhor’] * (param[’Neff’] + param[’Nmnu’] * rhonu)) / a**2
    + param[’grhom’] * param[’OmegaDE’] * (-3*(1+param[’w_DE_0’]+(1-a)*param[’w_DE_a’])*rho_Q * a**2 + 2 * rho_Q * a**2)
) * aprimeoa + param[’grhor’] * param[’Nmnu’] * rho_nu_prime / a**2


#aprimeoaprime = grhoprime/(6*aprimeoa)
aprimeoaprime = grhoprime/(2*jnp.sqrt(3)*jnp.sqrt(grho))
dgrho = (
    param[’grhom’] * (Omegac * deltac + param[’Omegab’] * deltab) / a
    + (param[’grhog’] * deltag + param[’grhor’] * (param[’Neff’] * deltar + param[’Nmnu’] * drhonu)) / a**2
    + param[’grhom’] * param[’OmegaDE’] * deltaq * rho_Q * a**2
)

dgpres = (
    (param[’grhog’] * deltag + param[’grhor’] * param[’Neff’] * deltar) / a**2 / 3.0
    + param[’grhor’] * param[’Nmnu’] * dpnu / a**2
    + (cs2_Q * param[’grhom’] * param[’OmegaDE’] * deltaq * rho_Q * a**2 + (cs2_Q-ca2_Q)*(3*aprimeoa * rho_plus_p_theta_Q / kmode**2))
)
dgtheta = (
    param[’grhom’] * (Omegac * thetac + param[’Omegab’] * thetab) / a
    + 4.0 / 3.0 * (param[’grhog’] * thetag + param[’Neff’] * param[’grhor’] * thetar) / a**2
    + param[’Nmnu’] * param[’grhor’] * kmode * fnu / a**2
    + rho_plus_p_theta_Q
)
dgshear = (
    4.0 / 3.0 * (param[’grhog’] * shearg + param[’Neff’] * param[’grhor’] * shearr) / a**2
    + param[’Nmnu’] * param[’grhor’] * shearnu / a**2
)
dgshearprime= (
    4.0 / 3.0 * (param[’grhog’] * sheargprime
                 + param[’Neff’] * param[’grhor’] * shearrprime) / a**2
    + param[’Nmnu’] * param[’grhor’] * shear_nu_prime / a**2
    - 2 * aprimeoa * dgshear
)
```

Listing 3.6: Defining the dark energy expressions, the neutrino metric perturbations and the standard metric perturbations

Furthermore, the metric potentials, along with the gauge transformation variable α must be defined as shown in List. 3.7.

```
hprime = (2.0 * kmode**2 * eta + dgrho) / aprimeoa
etaprime = youtprime[...,2]
alpha  = (hprime + 6.*etaprime)/2./kmode**2
alphaprime  = -3 * dgshear / (2 * kmode**2) + eta - 2 * aprimeoa * alpha
alphapprime = -3 * dgshearprime / (2*kmode**2) + etaprime - 2*
    aprimeoaprime * alpha  - 2*aprimeoa * alphaprime
```

Listing 3.7: Defining the metric potentials and the gauge transformation

From the perturbations, the polarization terms are computed as List.3.8.

```
polter = yout[:,:,idxg+2] + yout[:,:,idxgp+0] + yout[:,:,idxgp+2]
#polterprime  = yprime[:,:,idxg+2] + yprime[:,:,idxgp+0] + yprime[:,:,
    idxgp+2]
polterprime = 8/15 * (thetag + kmode**2 * alpha) - 3*kmode/5 *(yout[:,:,
    idxg+3] + yout[:,:, idxgp+1] + yout[:,:, idxgp+3]) - 3/10*opac*polter
couplprime   = 8*(thetagprime+kmode**2 * alphaprime)/15 - kmode*0.6*(
    yprime[:,:,idxg+3] + yprime[:,:,idxgp+1] + yprime[:,:,idxgp+3])
polterpprime = couplprime - 0.3 * (opacprime*polter + opac*polterprime)
```

Listing 3.8: Calculating the polarization terms from the perturbations

3.4 CMB spectrum code

The source function is calculated as shown in List. 3.9.

```
s1 = etaprime + alphapprime
s2 = 2 * alphaprime
expmmu = jnp.exp(-optical_depth)
S1 = expmmu*s1 # ISW
S2 = gvis*(0.25*deltag + s2 + polter/16+(thetabprime+3/16*polterpprime)/
    kmode**2) # SW
S3 = gvisprime *(alpha + (thetab + 3/8*polterprime) / kmode**2 ) #
    Doppler term
S4 = gvispprime * 3/16 * polter / kmode**2 # Polarization term
S=S1+S2+S3+S4
```

Listing 3.9: Calculating the Source function

The photon multipoles are then computed as shown in List. 3.10. The corresponding function is partially Jit compiled with l specified as a static argument. The integral is performed numerically using the JAX implementation of the trapezoid rule.

```
@partial(jax.jit, static_argnames=['ellmax'])
def get_thetal( ellmax, kmodes, tau ):
  tau0 = param['tau_of_a_spline'].evaluate(1.0)
  ktau = kmodes[:, None] * (tau0-tau[None, :])

  sj = spherical_bessel(ellmax, ktau.flatten())[:,0,:]
  sj = sj.reshape(len(kmodes), len(tau), ellmax+1, )
  integrand = sj * S[:, :, None]
```

```

  theta_l = jnp.trapezoid( integrand , x=tau , axis=-2 )
  return theta_l , integrand
ellmax = 2000
ell = jnp.arange(ellmax+1)
theta_l , integrand = get_thetal(ellmax , kmodes , tau)
```

Listing 3.10: Calculating the multipole moments

3.4.1 Anisotropy spectrum

The angular power spectrum is then computed using the JAX implementation of the trapezoidal integration method as shown in List.3.11. The result is expressed in terms of D_l, which is the most conventional form of plotting the CMB spectrum.

```
Cell = jnp.trapezoid((kmodes[:,None]/param['k_p'])**(param['n_s']-1)*jnp.abs(theta_l)**2, x=jnp.log(kmodes), axis=0 ) Dell = ell[2:] *(ell[2:]+1)*Cell[2:]*param['A_s']*4*jnp.pi/(2*jnp.pi) * param['Tcmb']**2
```

Listing 3.11: Calculating the CMB power spectrum

3.4.2 Anisotropy map

The CMB anisotopy map is generated using the python package healpy which is specifically designed for working with pixilated data on a sphere [22]. The procedure is shown in List.3.12. First, arrays of l and m are generated to define the spherical harmonics coefficient. Real and imaginary Gaussian variables are sampled and appropriately scaled to ensure that the a_{lm} coefficient have the correct variance. These real and imaginary part of a_{lm} are combined to form complex a_{lm} values. After that the CMB map is constructed by generating a random realization of a_{lm} directly from the computed power spectrum. Since healpy does not support jax arrays, the a_{lm} must be converted to numpy arrays. The last step is to perform an inverse spherical transform to transform a_{lm} into a real-space map of temperature anisotropies.

```
import healpy as hp
import numpy as np

Norm_Spec = Dell
def generate_alm_from_Cell(key, Norm_Spec , lmax):
    num_alm = hp.Alm.getsize(lmax) # Total number of a_lm values for l <= lmax
    ls , ms = hp.Alm.getlm(lmax) # Arrays of l and m corresponding to each a_lm index

    key1 , key2 = jax.random.split(key) # Split the PRNG key for real and imaginary parts
    # Sample standard Gaussian variables for real and imaginary parts
    # this is done since we can't directly sample imaginary gaussian variables
    gaussian_real = jax.random.normal(key1 , shape=(num_alm ,))
```

```
    gaussian_imag = jax.random.normal(key2, shape=(num_alm,))

    # Scale by sqrt(C_ell) to get the proper variance
    scalingreal = jnp.sqrt(Norm_Spec[ls])
    scalingimg = jnp.sqrt(Norm_Spec[ls]/2)
    alm_real = jnp.where(ms == 0, scalingreal * gaussian_real, jnp.sqrt(Norm_Spec[ls] / 2) * gaussian_real)
    alm_imag = jnp.where(ms == 0, 0.0, jnp.sqrt(Norm_Spec[ls] / 2) * gaussian_imag)


    # Combine into complex a_lm. m=0 modes are real by symmetry.
    alm = alm_real + 1j * alm_imag
    return alm

# Generate CMB map from power spectrum
def generate_cmb_map_from_Cell(Norm_Spec, nside=512, seed=0):
    lmax = len(Norm_Spec) - 1 # Determine maximum multipole
    key = jax.random.PRNGKey(seed) # Create reproducible random seed

    # Generate complex a_lm coefficients from C_ell
    alm = generate_alm_from_Cell(key, Norm_Spec, lmax)
    # Convert from JAX to NumPy for Healpy compatibility
    alm_np = jax.device_get(alm)
    # Inverse spherical harmonic transform: alm -> real-space map
    cmb_map = hp.alm2map(alm_np, nside=nside, lmax=lmax, verbose=False)
    return cmb_map
cmb_map = generate_cmb_map_from_Cell(Norm_Spec, nside=512, seed=0)

hp.mollview(cmb_map, title="CMB Anisotropy Map", cmap='jet', unit='$K$')
plt.show()
```

Listing 3.12: CMB anisotropy map

3.4.3 Gradient of the spectrum

Since the objective of this project is to develop a fully differentiable code for simulating the CMB power spectrum, the spectrum can now be differentiated with respect to any input cosmological parameters. To enable this, the entire computation of the spectrum is encapsulated in one function, which takes the parameter to be differentiated as the argument. In this case the derivative is calculated with respect to Ω_m by using JAX's forward mode automatic differentiation function jax.jacfwd. The implementation of this is shown in List.3.13.

```
from jax import jacfwd
# Compute spectrum and derivative
Omegam = 0.3099
Cell = compute_Cell(Omegam= 0.3099)
dCell_dOmegam = jacfwd(compute_Cell)(Omegam)
```

```
Gradient_Dl = Omegam * dCell_dOmegam[2:]/Cell[2:]*A_s*4*jnp.pi/(2*jnp.pi)
    * Tcmb**2
```

Listing 3.13: Gradient of the CMB spectrum with respect to Ω_m

3.5 Optimizing the code

After developing the code for computing the CMB spectrum, it is essential, to optimize its efficiency and speed for practical use. This involves identifying the sections of the code that require the most computational time and implementing strategies to reduce their runtime. After an investigation, it was found that the portion with sampling the modes, evolving the background and computing the perturbations outlined in List.3.1 takes approximately 70 s to run. The other inefficient part of the code is where the line-of-sight integral is computed, meaning the code shown in List.3.10, this part requires 170 s to run.

3.5.1 Interpolating

To reduce the computational cost, the number of sampled k-modes and scale factors is significantly reduced and then interpolated back to a higher number. Initially, $1024k$ modes are sampled linearly between 10^{-5} and 2, this is then reduced to 100 logarithmically spaced samples within the same range. The number of scale factor sampled during recombination between $3 \cdot 10^{-4}$ to $5 \cdot 10^{-3}$ is chosen to be 200 and 64 after recombination. To compute the source function, the k and a grids are interpolated by using the spline interpolation of DISCO-EB onto a finer linear grid. Specifically, the number of k modes is interpolated back to 1024, while the a grid is refined to 256 values during recombination and 300 afterwards. This interpolation process, as shown in List.3.14, reduced the runtime of this part of the code from 70 s to 39 s.

```
# Step 1: interpolate over k for each fixed x_j
# Input: S has shape (nk=100, nx=320), kmodes has shape (100,)
start_time = time.time()
k_fine = jnp.linspace(kmodes.min(), kmodes.max(), 1024)  #1024

# Interpolate each column (over k)
def spline_k(s_col):  # s_col is shape (100,)
    spline = spline_interpolation(kmodes, s_col)  # make spline over k
    return spline.evaluate(k_fine)

# Apply to each x_j (320 columns)
S_interp_k = vmap(spline_k, in_axes=1, out_axes=1)(S)  # shape (1024,
    320)

# Step 2: interpolate over a for each fixed k_i (row of S_interp_k)
aexp_out = jnp.geomspace(3e-4, 5e-3, 256, endpoint=False)  #256
aexp_out = jnp.append( aexp_out, jnp.geomspace(5e-3, 1.0, 300))
tau = jax.vmap( lambda a: param['tau_of_a_spline'].evaluate(a) )(aexp_out
    )
```

```
def spline_a(s_row):  # s_row is shape (320,)
    spline = spline_interpolation(a, s_row)  # make spline over x
    return spline.evaluate(aexp_out)              # same grid, or you
    could define x_fine

# Now S_interp_2D is a 2D cubic spline evaluation: S(k_fine[i], x[j])
S_interp_2D = vmap(spline_a, in_axes=0, out_axes=0)(S_interp_k)
```

Listing 3.14: Interpolating the logarithmically sampled k modes and scale factors a on a finer linear grid

3.5.2 Spherical Bessel functions

The implementation of the CMB spectrum used the spherical Bessel function implementation of DISCO-EB, however, the computation of these are not optimized for the execution on a GPU. For this reason, the line-of-sight integral is not computed very efficiently. A few strategies, that are explained in the following, have been tried to optimize the calculation of the line-of-sight integral for GPU execution.

Limber Approximation

One possible solution to this problem that was investigated, is to find a good enough approximation of the spherical Bessel function, which makes the calculation faster, but is still accurate enough to get a sufficient spectrum.
One very promising approximation is the Limber approximation, which uses the fact, that the first peak of the spherical Bessel functions dominates in any spherical Bessel transformation. This can be applied to large multipole moments ℓ, where the Bessel function is replaced by a Dirac delta function, that is centered at the first peak as Eq.3.1 [23].

$$j_l(x) \to \sqrt{\frac{\pi}{2l+1}}\delta^{(1)}(l+1/2-x) \tag{3.1}$$

In our case this becomes Eq.3.2

$$j_l[k(\eta_0-\eta)] \to \sqrt{\frac{\pi}{2l+1}}\delta(-k(\eta_0-\eta)+l+1/2) \tag{3.2}$$

This reduces the runtime significantly to 0.384 seconds. However, when computing the spectrum with this approximation, it becomes apparent, that the approximation is not sufficiently accurate for the power spectrum. The computed spectrum with the Limber approximation is shown in Fig.3.1

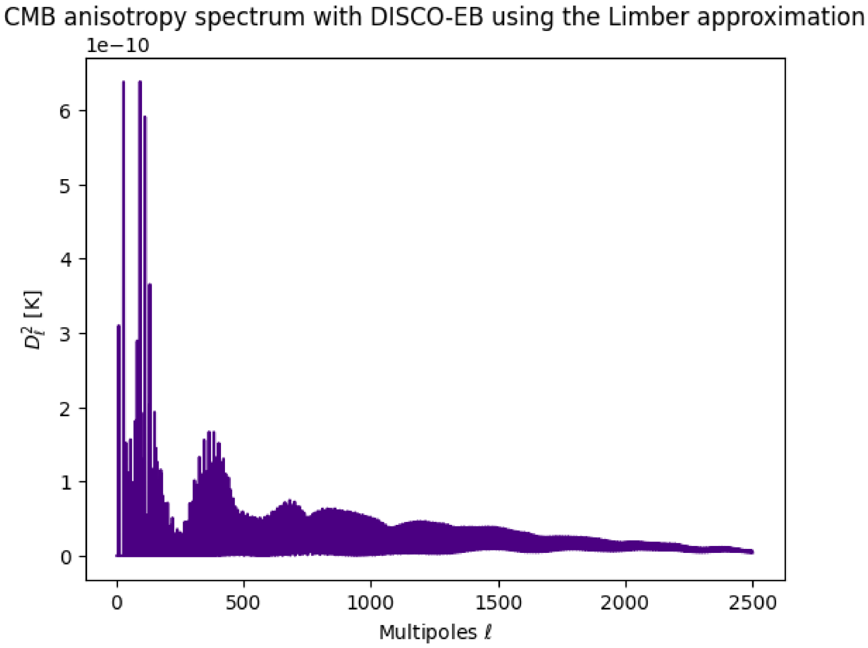

Figure 3.1: CMB Power spectrum calculated with DISCO-EB using the Limber approximation for the spherical Bessel functions in the Line-of-Sight integral.

The Limber approximation is mainly used for projected angular clustering of galaxies to the spatial clustering of galaxies in an approximate way. However, especially for large angular scales, this becomes increasingly more inaccurate. This manifests itself in the spectrum shown in Fig.3.1, where it can be seen, that it is very noisy [24].

Forward recursion

The method that was used in the end for optimizing the spherical Bessel functions, is forward recurrence, which enables maximum parallel efficiency and is therefore optimized for execution on a GPU. The relation for the forward recurrence is given as Eq.3.4 [25].

$$C_{\nu-1}(z) + C_{\nu+1}(z) = \frac{2\nu}{z} C_\nu(z) \tag{3.3}$$

$$C_{\nu-1}(z) - C_{\nu+1}(z) = 2C_\nu^{'}(z) \tag{3.4}$$

Since this is unstable for $|x| < \ell$, a continued fraction expansion has to be employed at these values, which uses Eq.[26].

$$\frac{J_\nu(z)}{J_{\nu-1}(z)} = \frac{1}{2\nu z^{-1}} - \frac{1}{2(\nu+1)z^{-1}} - \frac{1}{2(\nu+2)z^{-1}} - ... \tag{3.5}$$

Applying that for the spherical Bessel function gives Eq.3.6.

$$j_{n+1} = \frac{2n+1}{x} j_n - j_{n-1} \tag{3.6}$$

This significantly reduces the runtime from 170 seconds to 1.235 second.

4 Results

In this chapter, the results obtained from the implementation and testing of the DISCO-EB code for the CMB anisotropy are presented and their main implications summarized.

4.1 Recombination

Starting with recombination, for which the optical depth τ and the visibility function g were implemented. Their computation required the evaluation of the free electron fraction x_e, the electron number density n_e and the opacity.

4.1.1 Optical depth

Free electron fraction

The unitless free electron fraction x_e, extracted from the RECFAST recombination solver class in DISCO-EB, is shown as a function of conformal time η (in units of Mpc) in Fig.4.1. Conformal time $\eta = 1$ Mpc corresponds to the very early universe, while $\eta = 10^4$

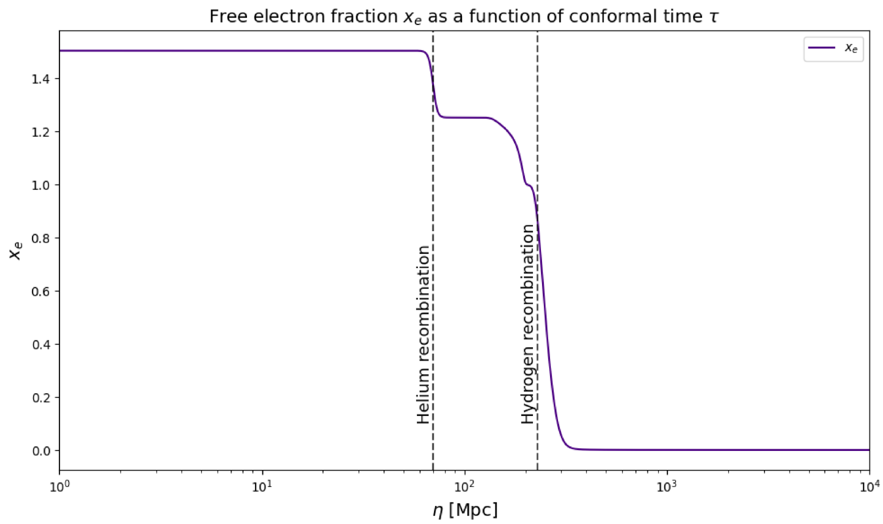

Figure 4.1: The free electron fraction x_e as a function of conformal time η (in Mpc), computed using the RECFAST class of DISCO-EB. The figure also highlights both Helium and Hydrgen recombination epochs.

Mpc represents the present day. In the early universe, the free electron fraction is roughly constant and exceeds 1, indicating a fully ionized plasma with a high density of free electrons. As the universe expands and cools, helium recombination occurs first, leading to a partial reduction in the number of free electrons. This is followed by hydrogen recombination, during which most of the remaining free electrons combine with protons to form neutral hydrogen. As a result, the free electron fraction rapidly drops to zero.

Electron number density

The electron number density n_e, which is directly related to the free electron fraction, is shown as a function of the scale factor a in a log-log plot in Fig.4.2. The electron number is given in units of electron per cubic meter (e^-/m^3), while the scale factor is dimensionless. Here $a = 10^{-5}$ corresponds to the early universe, and $a = 1$ the present day. As expected, the electron number density is highest in the early universe and steadily decreases as the universe expands. The small dip visible in the zoomed-in window corresponds to helium recombination, while the larger, more pronounced dip marks hydrogen recombination. During these epochs, free electrons combine with nuclei to form neutral atoms, significantly reducing the electron number density.

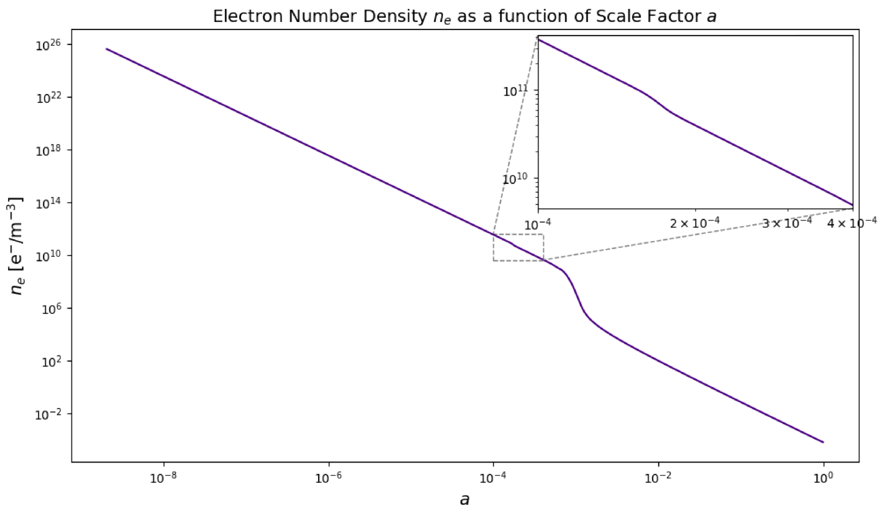

Figure 4.2: Electron number density n_e as a function of scale factor a in log-log scale. The plot highlights the epochs of helium and hydrogen recombination.

Opacity and optical depth

With the electron fraction x_e and the number density n_e computed, the opacity (in units of Mpc^{-1}) and the optical depth (unitless) can be evaluated. These are shown in Fig.4.3 as functions of $x = \ln a$, where $x = -20$ corresponds to the early universe and $x = 0$ to the present time. In the early universe, the high density of free electrons made the medium highly opaque to photons. Frequent Thompson scattering events caused the universe to be optically thick, meaning photons could not travel freely. As the universe expanded and cooled number, recombination occurred, binding most free electrons in neutral atoms. This lead to a sharp drop in the opacity. At recombination, most photons experienced their last scattering event. From that point onward, the universe became optically thin, allowing photons to travel freely.

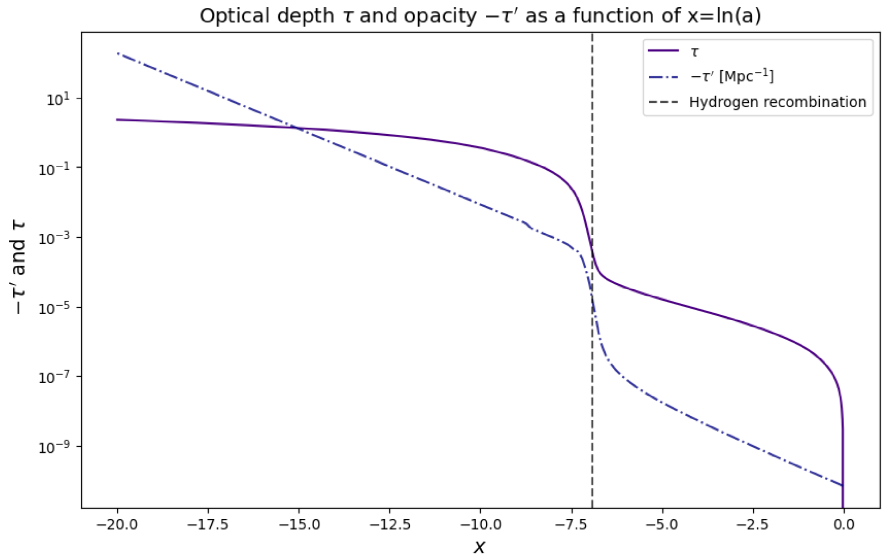

Figure 4.3: Opacity $-\tau$ in Mpc^{-1} and the unitless optical depth τ as functions of $x = \ln a$. The drop in both quantities reflects the transition from an optically thick to an optically thin universe during hydrogen recombination.

4.1.2 Visibility function and derivatives

From the optical depth, the visibility function (in units of Mpc^{-1}) can be computed. This is shown as a function of $x = \ln a$ in Fig.4.4. The visibility function describes the probability of photons scattering at each conformal time. It is nearly zero at all times expect during recombination, where it showcases a sharp peak. This peak corresponds is to the last-scattering surface.
The first and the second derivatives of the visibility function in units of Mpc^{-2} and Mpc^{-3} respectively are shown in Fig.4.5

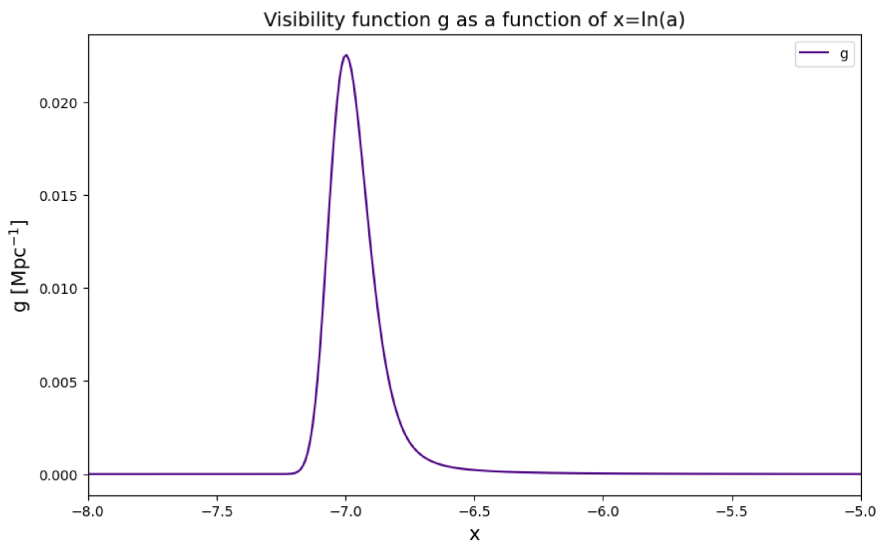

Figure 4.4: Visibility function g in Mpc^{-1} as a function of $x = \ln a$. The sharp peak indicates the last-scattering surface during hydrogen recombination.

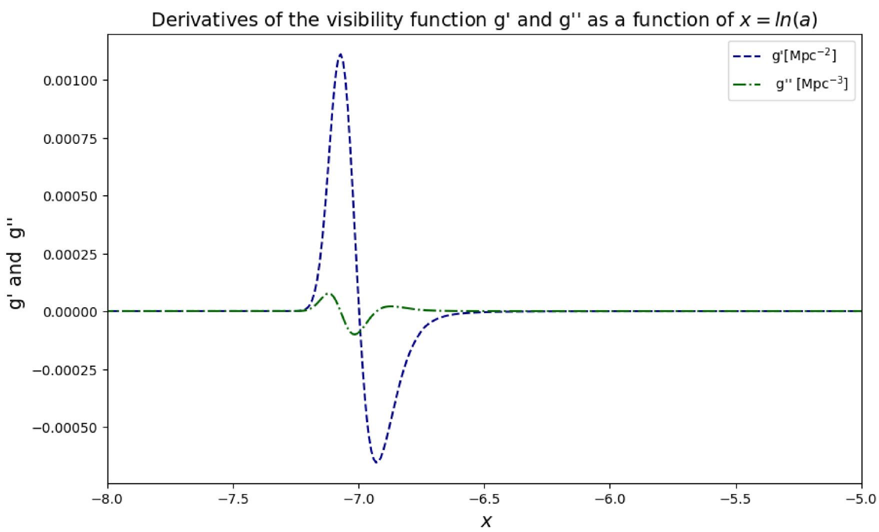

Figure 4.5: First and second derivatives of the visibility function g' and g'' in units of Mpc^{-2} and Mpc^{-3} respectively.

4.2 Line-of-Sight integral

The next set of results presented are obtained from the line-of-sight integral computation. This includes the evaluation of the source function $S(k, \eta)$, the resulting integrand of the line of sight integral, and the computed photon multipoles $\Theta_\ell(k)$.

4.2.1 Source function

The source function in units of Mpc^{-2} is computed as a function of the Fourier modes k with units Mpc^{-2} and the scale factor a. The result is displayed in Fig.2.82 as a 2D plot The plot shows a narrow, sharply defined band centered around $a \approx 10^{-3}$, corresponding

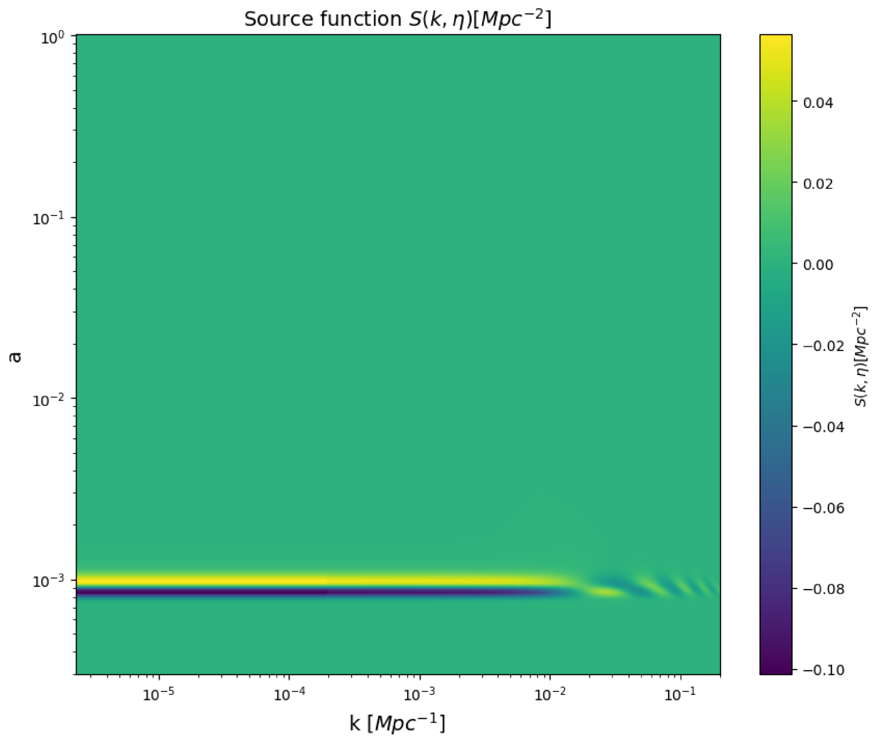

Figure 4.6: 2D image of the Source function $S(k, \eta)$ in Mpc^{-2}, plotted as a function of k with units Mpc^{-1} on the horizontal axis and a on the vertical axis.

to the epoch of recombination. This is the surface of last scattering, where most of the CMB anisotropies are sourced. At higher values of k, an oscillatory pattern is observed, which reflects the baryonic acoustic oscillations. These oscillations in the photon-baryon fluid ultimately produce the acoustic peaks in the CMB.

4.2.2 Photon multipoles

The integrand of the line-of-sight integral is given by the product of the source function $S(k,\eta)$ in units of Mpc^{-2} and the unitless spherical Bessel functions $j_\ell[k(\eta_0-\eta)]$. This is shown in Fig.4.7 as a function of $x = \ln a$ This plot reveals a sharp and prominent peak

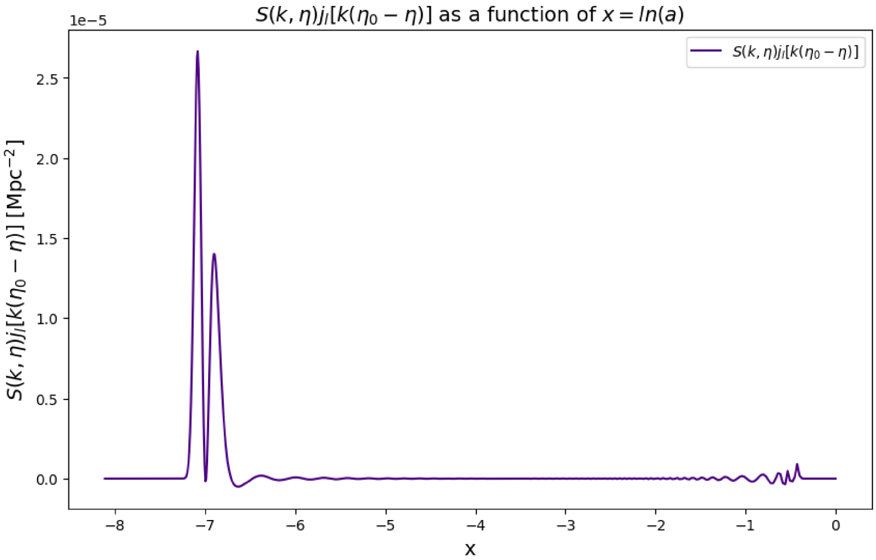

Figure 4.7: Integrand of the line-of-sight integral $S(k,\eta)j_l[k(\eta_0-\eta)]$ in units of Mpc^{-2} as a function of x.

at $x \approx -7$, associated with the peak of the source function during recombination. The spherical Bessel functions modify the peak by introducing oscillations centered at the peak. After the main peak, the integrand shows rapidly decaying oscillations, which reflects the contribution of the Bessel functions, that continue to oscillate for large arguments.
Finally, the photon multipoles $\Theta_\ell(k)$ in units of Mpc^{-1}, which are the result of the line-of-sight integral are shown in Fig.4.8 as a function of k in units of Mpc^{-1} and multipoles ℓ.

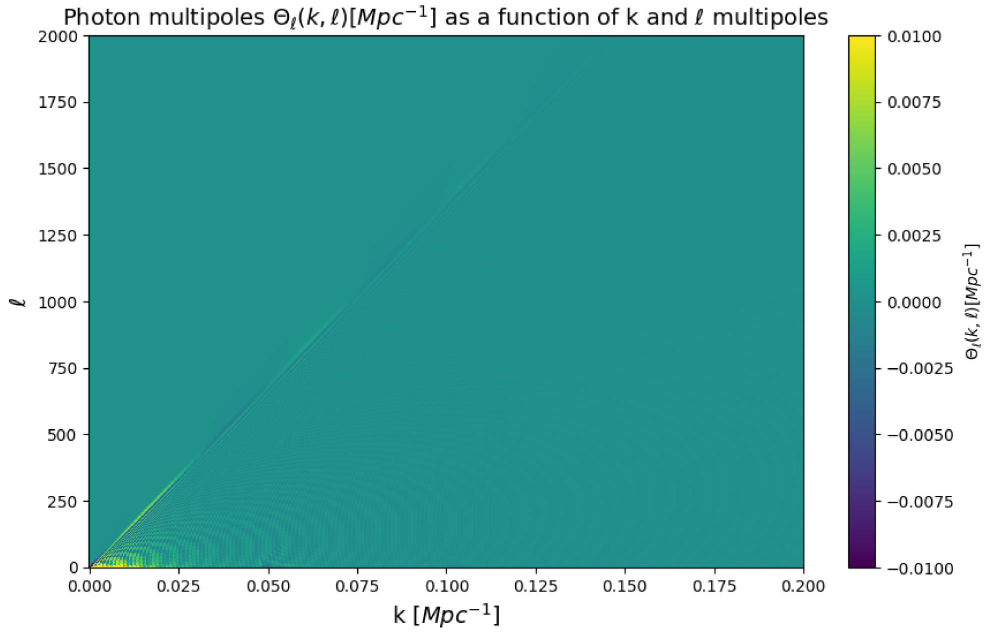

Figure 4.8: 2D plot of the photon multipoles $\Theta_\ell(k)$ in Mpc^{-1} as a function of k in Mpc^{-1} on the horizontal axis and the unit-less multipoles ℓ on the vertical axis.

In the plot a strong diagonal structure is visible along the curve $\ell \approx k(\eta_0 - \eta)$. Furthermore, at low k and ℓ an oscillatory structure can be seen, which once again corresponds to the acoustic oscillations in the photon-baryon fluid before recombination.

4.3 CMB power spectrum

The main result of this work is the angular CMB temperature-temperature anisotropy power spectrum. The final version of the spectrum is shown in Fig.4.9, where the normalized spectrum $D_\ell = \frac{\ell(\ell+1)}{2\pi}$ is plotted in units $[\mathrm{K}^2]$ as a function of multipoles ℓ.
The spectrum is shaped by primordial initial conditions at low multipoles, which corresponds to large angular scales. At these scales, the fluctuations were still outside the horizon at the time of photon decoupling, which leads to them not having evolving prior to this epoch and thus providing a direct imprint of the initial conditions of the universe. At intermediate multipoles, the spectrum is characterized by the sound waves in the photon-baryon fluid. These arise from perturbations with shorter wavelengths that entered the horizon before recombination. As the different modes evolved, they behaved like sound waves traveling through the tightly coupled photon-baryon fluid. The observed CMB captures these oscillations at various phases, since their oscillation frequency depends on their wavelength. At large multipoles corresponding to small angular scales, damping effects becomes significant. This damping is caused by the random diffusion of photons, which smooths out the density fluctuations in the plasma. Consequently, the amplitude

of the acoustic oscillations is suppressed at these scales [5].

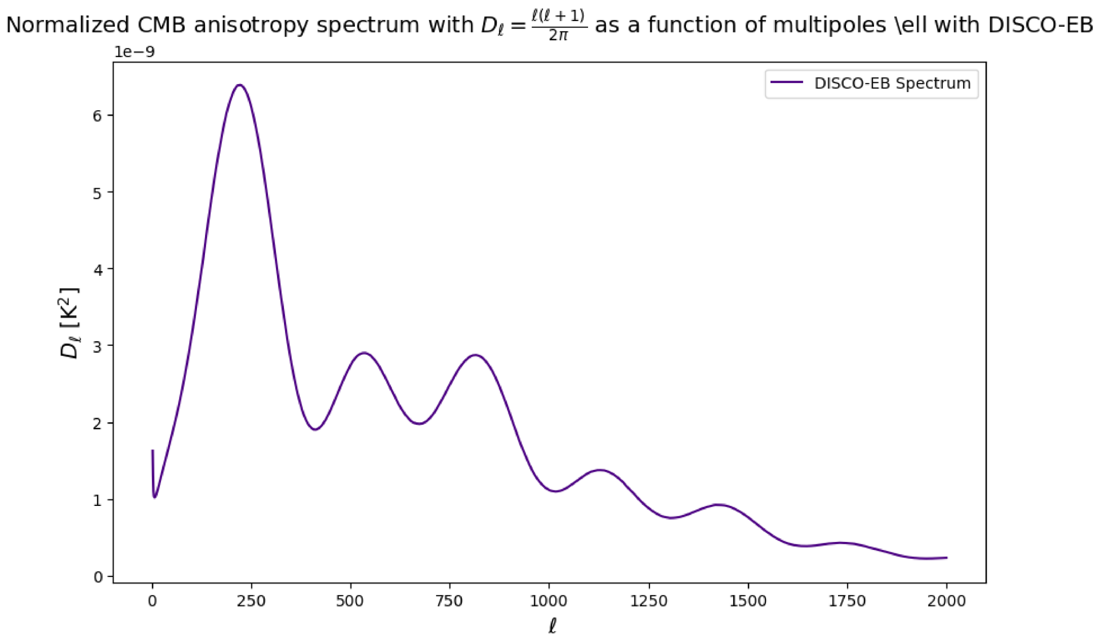

Figure 4.9: Normalized angular CMB temperature-temperature anisotropy power spectrum $D_\ell = \frac{l(l+1)}{2\pi}$ in units of K^2 plotted against multipoles ℓ.

4.4 Anisotropy map

A CMB anisotropy map can be generated by producing a Gaussian realization on the sky based on the calculated angular power spectrum. One Gaussian realization is shown in Fig.4.10. The map shows the temperature fluctuations in the CMB across the sky. The color scale in units of K represents the deviations from the mean CMB temperature, where the blue regions represent cooler spots and the red regions indicate hotter spots. One can now also extract the angular power spectrum directly from the generated sky realization. Here, since the map is only one realization, it is useful to average over a number of realizations to minimize statistical uncertainties like cosmic variance. Here 50 realizations are chosen to average over. In Fig.4.11 the mean and the standard derivation $\pm 1\sigma$ of the recovered spectrum is compared to the theoretical spectrum

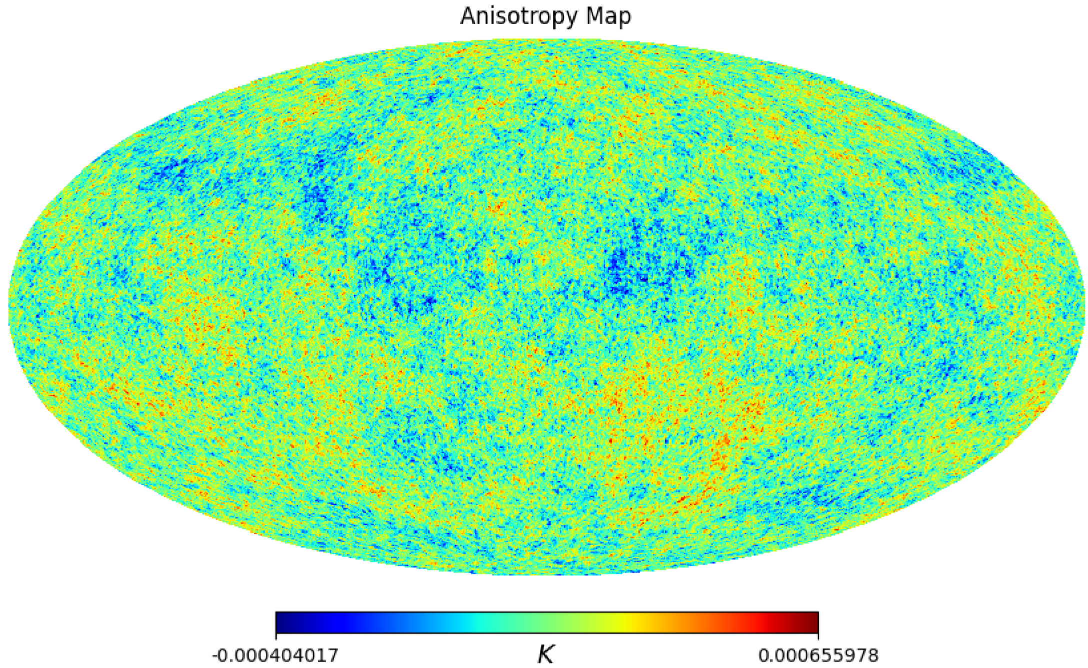

Figure 4.10: Full-sky CMB temperature anisotropy map generated from the simulated spectrum using the DISCO-EB outputs.

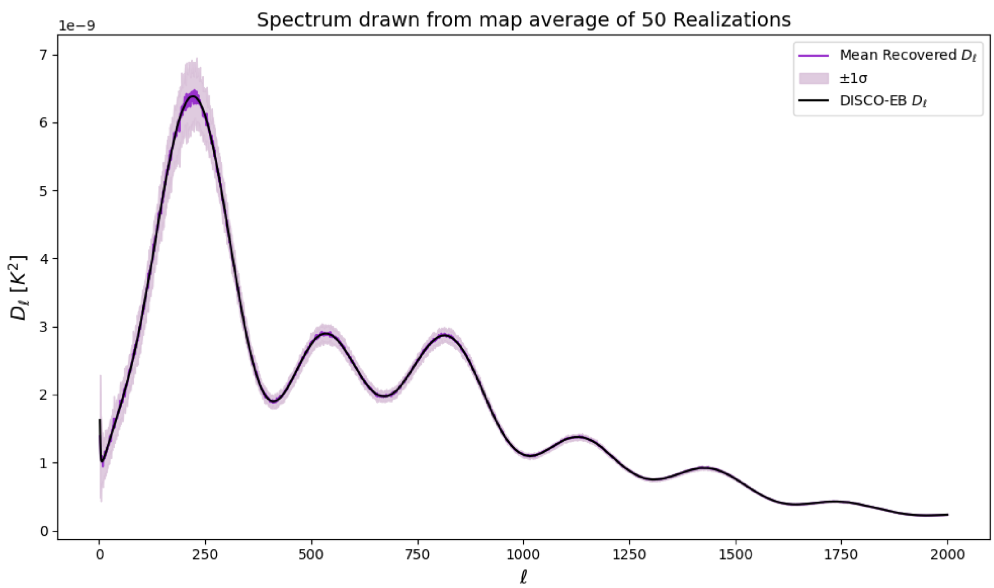

Figure 4.11: Recovered spectrum from averaging over 50 Gaussian realizations and $\pm 1\sigma$ standard derivation compared to the theoretically computed spectrum.

What can be seen here is, that the generated spectrum aligns well with the theoretical spectrum on all scales.

4.5 Gradient of spectrum

The code used to simulate the CMB power spectrum is fully differentiable. To demonstrate this, the gradient of the spectrum is calculated with respect to Ω_m using JAX's automatic differentiation. This result is then compared to a finite-difference approximation, where the finite difference is evaluated using the values $\Omega_m \pm 10^{-1}\Omega_m \pm 10^{-2}$ and $\Omega_m \pm 5 \cdot 10^{-3}$ as the offset. This comparison is shown in Fig.4.12. The derivatives are only computed up

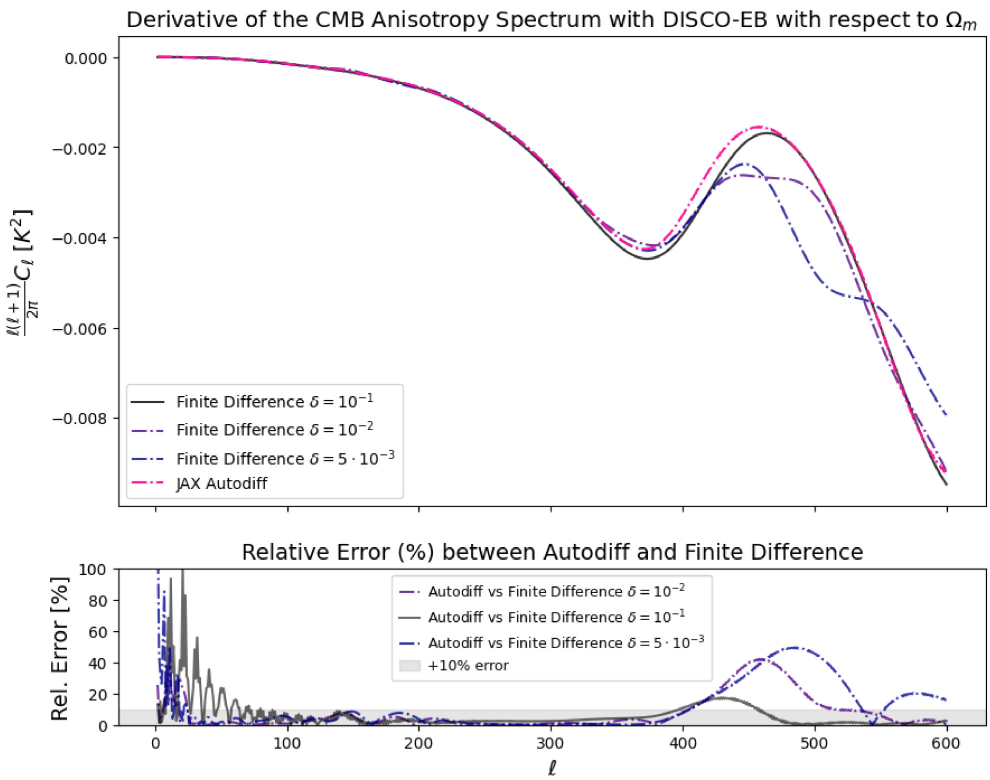

Figure 4.12: Gradient of the CMB power spectrum with JAX automatic differentiation compared to computing the derivative through finite differences with respect to Ω_m and the relative error of the different methods.

to $\ell_{max} = 600$ due to the high computational cost of evaluating gradients. The derivative of the CMB temperature power spectrum with respect to Ω_m reveals how sensitive the spectrum is to changes in Ω_m. At low multipoles, the derivative decreases gradually, indicating that an increase of Ω_m leads to a decrease in the amplitude of the spectrum at larger scales. Physically, an increase of Ω_m corresponds to a universe with more matter content, meaning matter domination is reached earlier. This results in suppression of the

evolution of the gravitational potentials, reducing the contribution of the early ISW effect. The derivative then rises and a peak is reached between about $\ell = 400$ and $\ell = 500$, close to the location of the second acoustic peak of the spectrum. This feature most likely corresponds to the horizontal shift of the acoustic peaks towards smaller angular scales caused by an increase in Ω_m. After that the derivative decreases again, the sensitivity to the effects of Ω_m becomes less pronounced.
Another notable observation is that the derivative of the CMB power spectrum with respect to Ω_m computed via finite differences appears significantly less smooth than the one obtained through automatic differentiation. This discrepancy is particularly evident at low multipoles and around the first acoustic peak, where the errors become large. Interestingly, using a relatively large finite difference step size $\delta = 10^{-1}$ yields the smallest error near the acoustic peak. However, the same step size leads to numerical artifacts at low multipoles, where the derivative of the spectrum is mostly 0 and the relative error measurements break down.
On the other hand, the smallest finite difference step size of $\delta = 5 \cdot 10^{-3}$ also results in large errors.
In contrast, automatic differentiation computes the exact gradient accounting for all nonlinear dependencies. This essentially results in a smoother and more precise curve, especially in regions where the spectrum is highly sensitive to changes in the given parameter, which makes it a more suitable approach than finite differences in this case.
Of course the derivatives can also be taken with respect to other cosmological input parameters. In Fig.4.13, the gradient of the CMB power spectrum with respect to the baryon density Ω_b is shown, computed using both JAX automatic differentiation and the finite difference method with step sizes $\delta = 10^{-2}$ and $5 \cdot \delta = 10^{-3}$. It becomes evident here, that the first and second acoustic peaks are highly sensitive to changes in Ω_b reflecting the strong impact of baryon density on the amplitude of acoustic oscillations in the photon-baryon fluid. Increasing Ω_b leads to an increase in the amplitude of the odd-numbered peaks and to a decrease of the amplitude of the even-numbered peaks.
Overall the relative error between the two approaches stays relatively small over large ranges of multipoles. However the error spikes at around $l \approx 20$, $l \approx 400$ and $l \approx 600$. These correspond to regions where the derivative is exactly 0, hence where the relative error calculation fails due to division by 0.

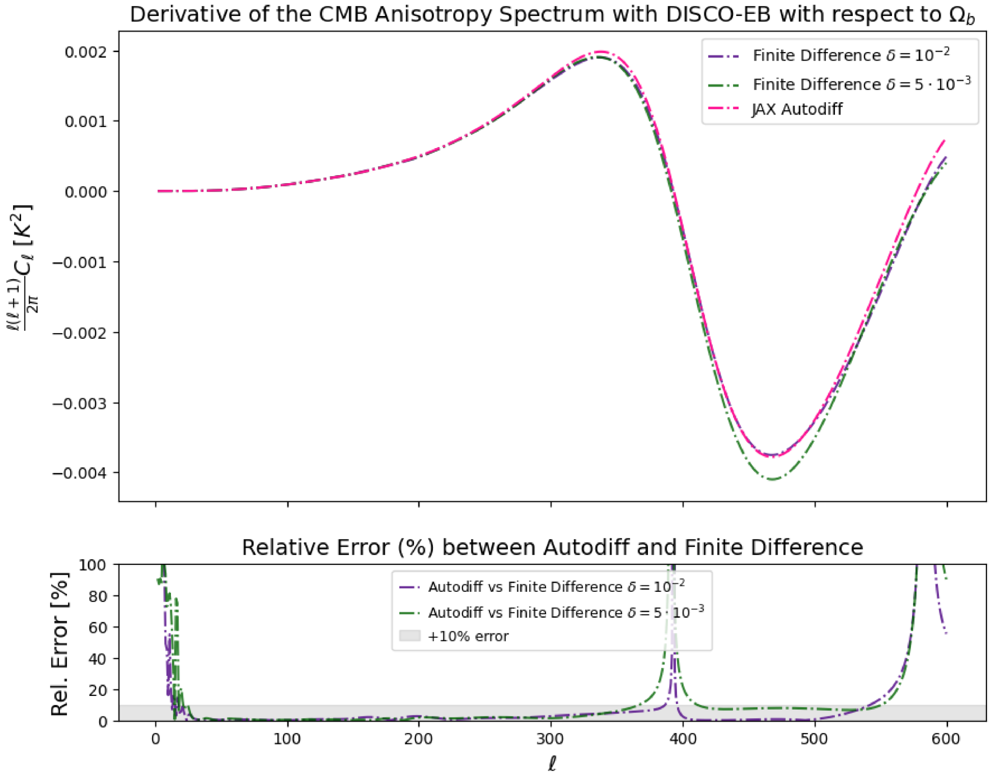

Figure 4.13: Gradient of the CMB power spectrum with JAX automatic differentiation compared to computing the derivative through finite differences with respect to Ω_b and the relative error of the different methods.

The derivative with respect to the scalar index n_s is shown in Fig.4.14, where once again the automatic differentiation method is compared to finite differences with step size $\delta = 10^{-1}$, $\delta = 10^{-2}$ and $\delta = 10^{-3}$. What can be seen here, is that increasing n_s leads to a suppression of the first acoustic peak, while enhancing the amplitude of the spectrum at smaller scales. The agreement between the different approaches is good at all considered mutlipoles in this case, with only a comparatively small spike for the $\delta = 10^{-2}$ finite difference case observed at $l \approx 550$, which once again corresponds to a numerical artifact due to the derivative reaching 0.

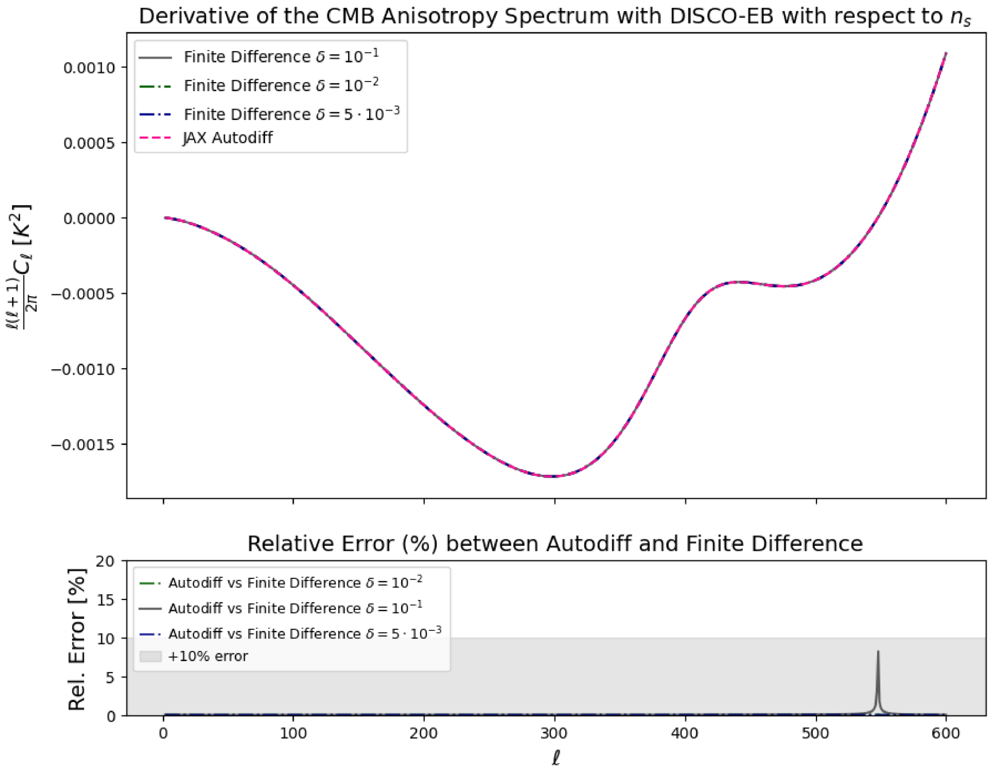

Figure 4.14: Gradient of the CMB power spectrum with JAX automatic differentiation compared to computing the derivative through finite differences with respect to n_s and the relative error of the different methods.

The derivative with respect to the dark energy equation of state parameter w_0 is shown in Fig.4.15, the derivative shows that on large scales, the spectrum is relatively insensitive to an increase of w_0, while at smaller scales the amplitude of the first acoustic peak increases and the amplitude of the second one gets suppressed. The relative error remains relatively small overall but exhibits noticeable numerical artifacts due to division by zero.

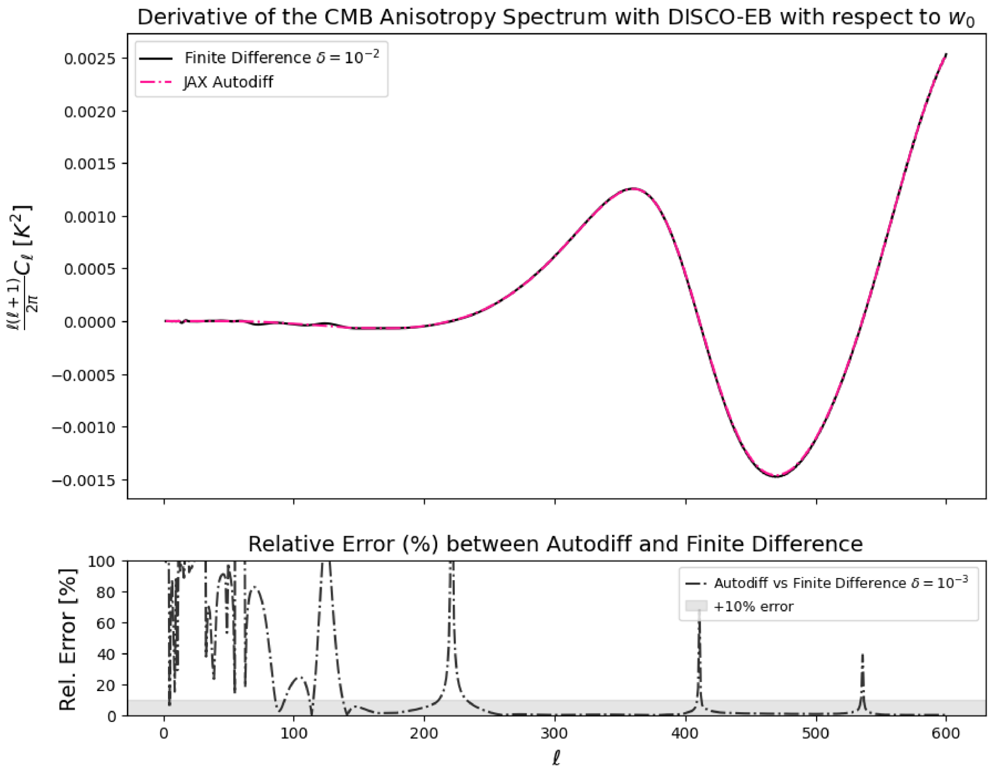

Figure 4.15: Gradient of the CMB power spectrum with JAX automatic differentiation compared to computing the derivative through finite differences with respect to w_0 and the relative error of the different methods.

5 Discussion

5.1 Comparison with CAMB

To validate the accuracy of the CMB power spectrum computed with DISCO-EB, it is useful to compare it against a reference spectrum obtained using a well established Einstein-Boltzmann solver such as CAMB. This is shown in Fig.5.1 Between $\ell = 100$ and

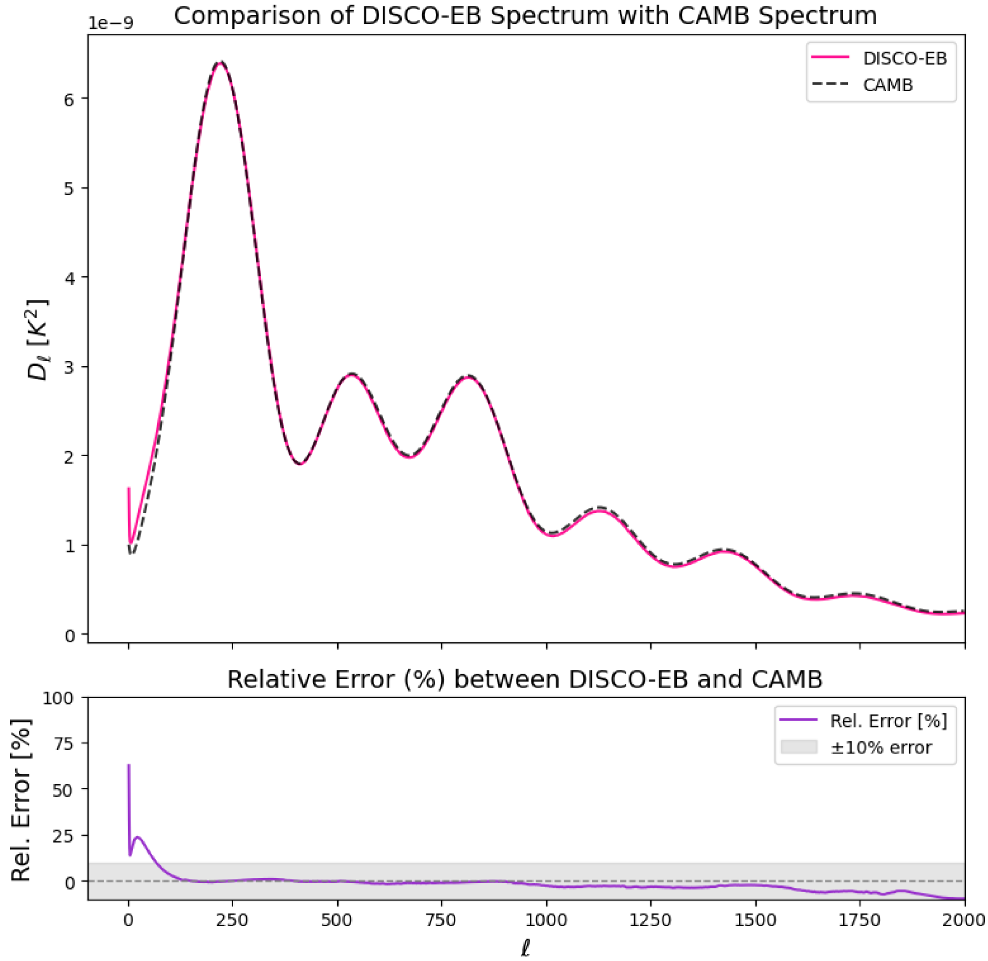

Figure 5.1: Comparison of the CAMB and the DISCO-EB spectrum and the relative error between them.

$\ell = 1000$, the DISCO-EB and CAMB spectra are in good agreement, with a maximum relative error of about 3 %. This indicates, that in the intermediate multipole range when the acoustic peaks are most prominent, DISCO-EB accurately reproduces the expected angular power spectrum.
At lower multipoles ($\ell < 100$), however, the spectra show significant divergence. The largest relative error occurs at $\ell = 0$, reaching approximately 63 %. This suggests either a numerical instability or a systematic error in the treatment of the largest angular scales. As of now, no conclusive solution has been found for this discrepancy.
At higher multipoles $\ell > 1000$ the spectra also begin to diverge, though less significantly. Here the relative error is consistently negative, indicating that DISCO-EB underestimates the spectrum compared to CAMB. The maximum absolute value of the relative error in this regime is around 9 %. This underestimation arises from the choice of $k_{max} = 2$, which is insufficient to fully capture the contributions to the spectrum at high multipoles. Increasing k_{max} to for example 5 improves the theoretical coverage but introduces significant numerical noise across the entire spectrum. This could be due to the limited resolution of the k grid $n = 1024$, which is already near the current computational limit.
The discrepancy at low ℓ becomes more apparent when the spectra are plotted in a logarithmic scale. Here is becomes evident, that the so called Sachs-Wolfe plateau is significantly overshot with DISCO-EB. This behavior is shown in Fig.5.2.

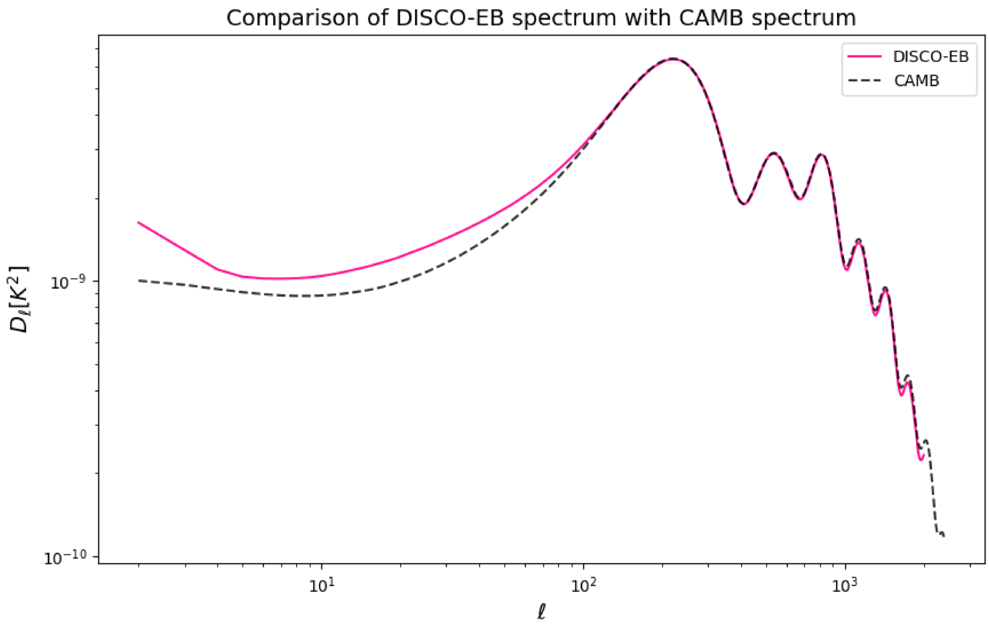

Figure 5.2: Comparison of the spectra in logarithmic space.

Another important point of comparison is the derivatives of the CMB power spectrum with respect to cosmological parameters. Fig.5.3 compares the derivatives of the spectra with respect to Ω_m computed by DISCO-EB using finite differences with $\delta = 10^{-2}$ as an offset and automatic differentiation to the one obtained from CAMB's finite difference with $\delta = 10^{-3}$ as an offset. What can be seen in the upper plot is that the three method closely follow one another, apart from the finite difference approach of DISCO-EB that diverges at the peak. The relative error shows that at low multipoles, the error is significantly larger, which could be due to numerical inaccuracies. Interestingly, the relative error between CAMB and DISCO-EBs auto diff remains very low for most ℓ.
In Fig.5.4 the comparison of the derivatives with respect to Ω_b is shown. Here the

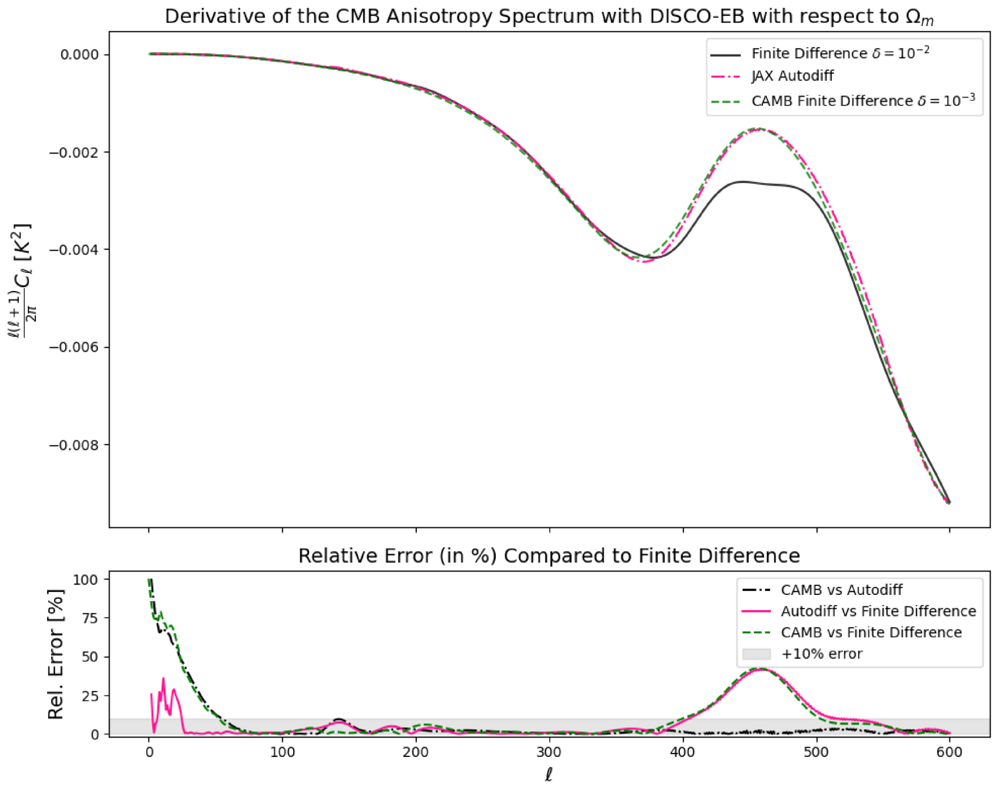

Figure 5.3: Comparison of the auto differentiation method of DISCO-EB to the finite differences of DISCO-EB and CAMB and the respective relative errors for the derivative with respect to Ω_m.

DISCO-EB approaches both are in good agreement with the CAMB finite difference approach. The large error spikes once again correspond to numerical artifacts generated by division by 0.

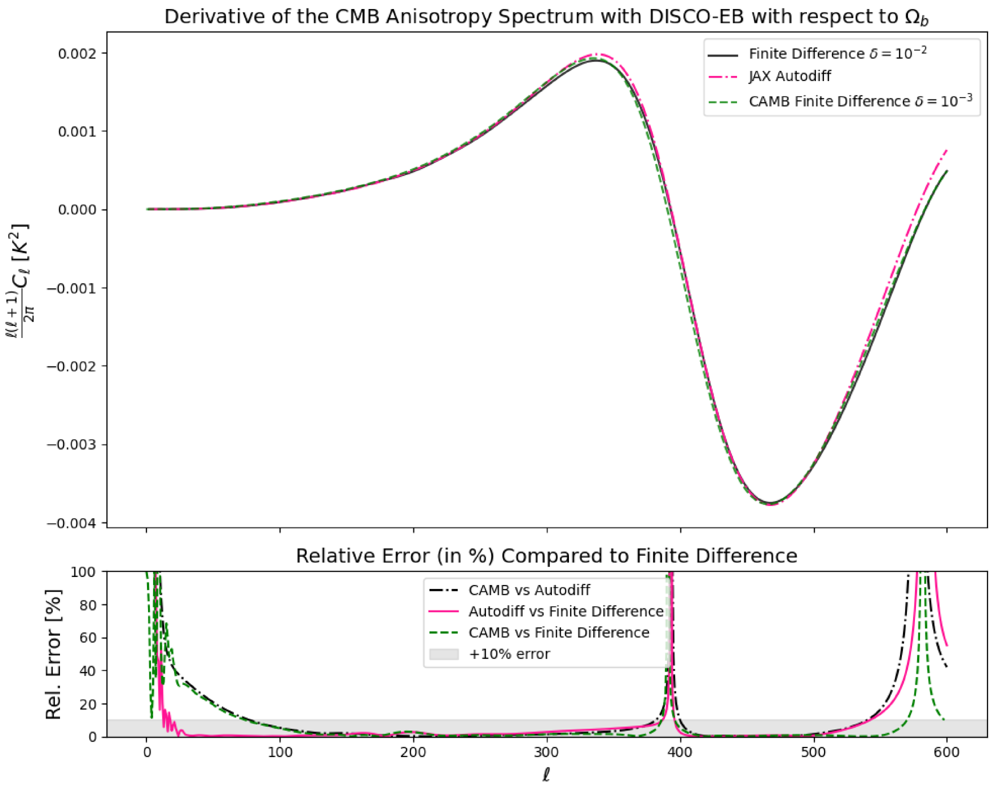

Figure 5.4: Comparison of the auto differentiation method of DISCO-EB to the finite differences of DISCO-EB and CAMB and the respective relative errors for the derivative with respect to Ω_b.

In Fig.5.5 the same comparison is presented for the derivatives with respect to the scalar spectral index n_s. At low multipoles, the derivatives computed by DISCO-EB and CAMB show good agreement, however, at higher multipoles, the CAMB derivative slightly overshoots those obtained from DISCO-EB. This could be due to differences in how the two codes handle small-scale resolution.

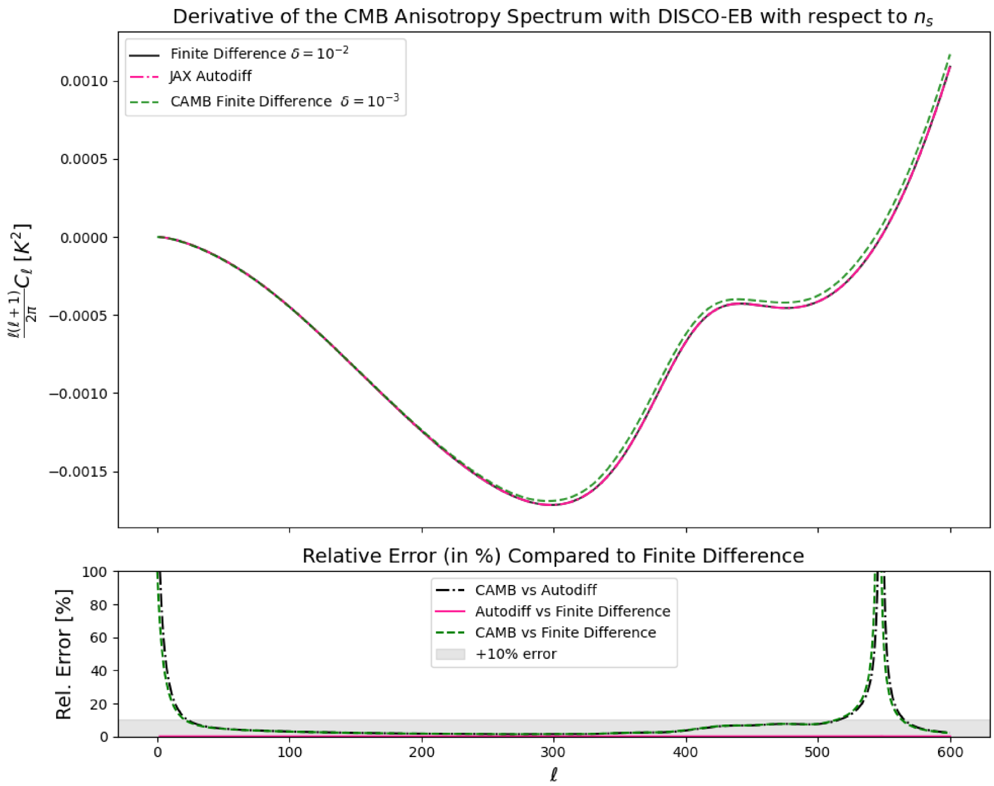

Figure 5.5: Comparison of the auto differentiation method of DISCO-EB to the finite differences of DISCO-EB and CAMB and the respective relative errors for the derivative with respect to n_s.

In Fig.5.6 the comparison to CAMB is shown for the derivatives with respect to w_0, which overall shows a good agreement between the two codes, apart from the numerical artifacts that are very present.

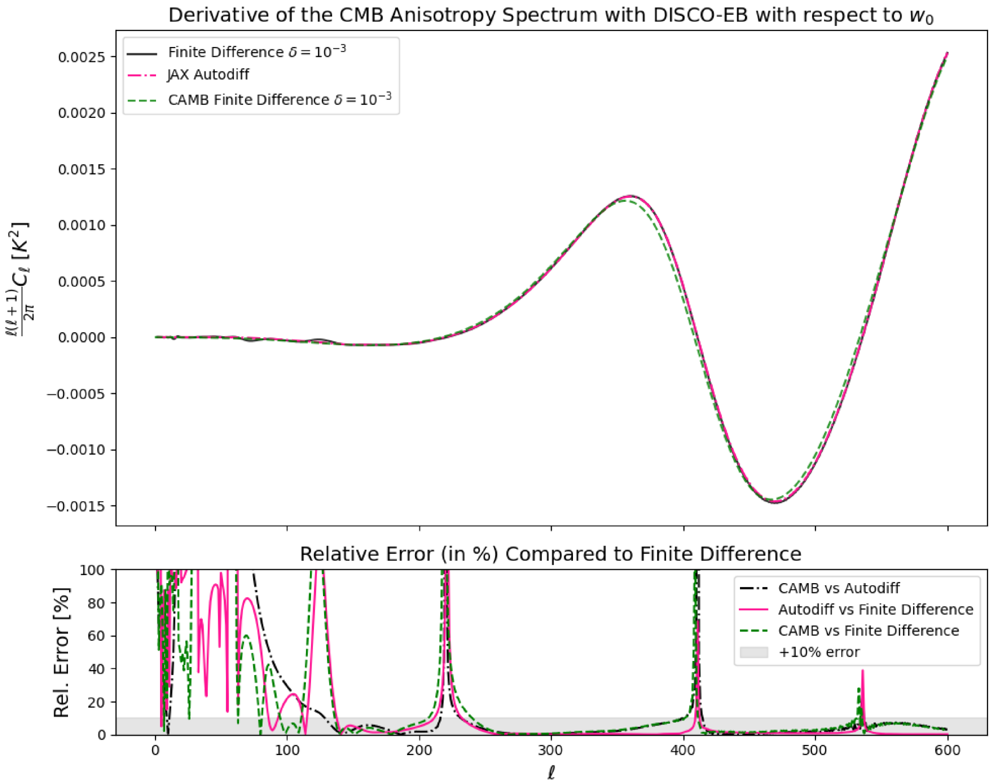

Figure 5.6: Comparison of the auto differentiation method of DISCO-EB to the finite differences of DISCO-EB and CAMB and the respective relative errors for the derivative with respect to w_0.

6 Outlook

Future work to further improve and expand this research, such as developing it into a PhD project, could focus on enhancing the physical completeness of the current model by incorporating additional cosmological effects such as CMB lensing and reionization. Including CMB lensing would significantly improve the accuracy of the predicted power spectra and maps, while modeling reionization would account for photon scattering in the late Universe, which also leaves an imprint on the CMB anisotropies.
On the computational side, there remains substantial room for improvement through optimization of numerical routines and the implementation of more GPU acceleration strategies.hese advances would reduce runtime and therefore enable higher-resolution simulations. Additionally, future efforts could aim to integrate the model within cosmological inference frameworks.
Another extension of this work is implementing a method to generate polarization spectra and maps. Adding polarization capabilities would further deepen the scientific utility of the model.

7 Conclusion

The objective of this thesis was to develop a numerical code to simulate the Cosmic Microwave Background (CMB) temperature anisotropies using the output of the fully differentiable Einstein-Boltzmann Solver DISCO-EB [2] written in the JAX framework and developed by the Vienna cosmology group in recent years. This was achieved by implementing a method to compute the angular temperature-temperature anisotropy spectrum of the CMB using the line-of-sight formalism. In this approach, sources of anisotropy along the line-of-sight of an observer are expanded in multipoles and projected onto the two-dimensional sky via integration.

The resulting CMB spectrum achieves an accuracy comparable to that of the well established Solver CAMB across a broad range of angular scales. Additionally, it allows for the generation of realistic Gaussian CMB sky maps based on this spectrum.

A key innovation of this work is that, due to DISCO-EB being fully differentiable, the computed CMB power spectrum is also fully differentiable. This makes it possible to take exact derivatives of the spectrum with respect to any cosmological input parameter, making this the first known CMB code capable of automatic differentiation. Differentiability has increasingly become important to the cosmological community, as it enables to assess the sensitivity of cosmological models to the input parameters and very efficient Bayesian inference.

However, this work is not without limitations. The computed spectrum is still not fully accurate on all angular scales, particularly at very small and very large multipoles. Moreover, the runtime of the code could not be reduced below approximately 40 seconds, which limits its applications.

Future work could focus on extending the physical completeness of the model. For example, CMB lensing or reionization are not included yet in the model and could increase its accuracy. Furthermore, a more thorough investigation of numerical routines and GPU acceleration strategies could still reduce runtime significantly.

Bibliography

[1] A. Lewis and S. Bridle, "Camb: Code for anisotropies in the microwave background." `https://github.com/cmbant/CAMB`, 2025. Accessed: 2025-07-06.

[2] O. Hahn, "Disco-eb: Differentiable simulations of the cosmic microwave background." `https://github.com/ohahn/DISCO-EB`, 2024. Accessed: 2025-06-19.

[3] O. Hahn, F. List, and N. Porqueres, "Disco-dj i: a differentiable einstein-boltzmann solver for cosmology," *Journal of Cosmology and Astroparticle Physics*, vol. 2024, p. 063, June 2024.

[4] N. Aghanim, Y. Akrami, M. Ashdown, J. Aumont, C. Baccigalupi, M. Ballardini, A. J. Banday, R. B. Barreiro, N. Bartolo, S. Basak, R. Battye, K. Benabed, J.-P. Bernard, M. Bersanelli, P. Bielewicz, J. J. Bock, J. R. Bond, J. Borrill, F. R. Bouchet, F. Boulanger, M. Bucher, C. Burigana, R. C. Butler, E. Calabrese, J.-F. Cardoso, J. Carron, A. Challinor, H. C. Chiang, J. Chluba, L. P. L. Colombo, C. Combet, D. Contreras, B. P. Crill, F. Cuttaia, P. de Bernardis, G. de Zotti, J. Delabrouille, J.-M. Delouis, E. Di Valentino, J. M. Diego, O. Doré, M. Douspis, A. Ducout, X. Dupac, S. Dusini, G. Efstathiou, F. Elsner, T. A. Enßlin, H. K. Eriksen, Y. Fantaye, M. Farhang, J. Fergusson, R. Fernandez-Cobos, F. Finelli, F. Forastieri, M. Frailis, A. A. Fraisse, E. Franceschi, A. Frolov, S. Galeotta, S. Galli, K. Ganga, R. T. Génova-Santos, M. Gerbino, T. Ghosh, J. González-Nuevo, K. M. Górski, S. Gratton, A. Gruppuso, J. E. Gudmundsson, J. Hamann, W. Handley, F. K. Hansen, D. Herranz, S. R. Hildebrandt, E. Hivon, Z. Huang, A. H. Jaffe, W. C. Jones, A. Karakci, E. Keihänen, R. Keskitalo, K. Kiiveri, J. Kim, T. S. Kisner, L. Knox, N. Krachmalnicoff, M. Kunz, H. Kurki-Suonio, G. Lagache, J.-M. Lamarre, A. Lasenby, M. Lattanzi, C. R. Lawrence, M. Le Jeune, P. Lemos, J. Lesgourgues, F. Levrier, A. Lewis, M. Liguori, P. B. Lilje, M. Lilley, V. Lindholm, M. López-Caniego, P. M. Lubin, Y.-Z. Ma, J. F. Macías-Pérez, G. Maggio, D. Maino, N. Mandolesi, A. Mangilli, A. Marcos-Caballero, M. Maris, P. G. Martin, M. Martinelli, E. Martínez-González, S. Matarrese, N. Mauri, J. D. McEwen, P. R. Meinhold, A. Melchiorri, A. Mennella, M. Migliaccio, M. Millea, S. Mitra, M.-A. Miville-Deschênes, D. Molinari, L. Montier, G. Morgante, A. Moss, P. Natoli, H. U. Nørgaard-Nielsen, L. Pagano, D. Paoletti, B. Partridge, G. Patanchon, H. V. Peiris, F. Perrotta, V. Pettorino, F. Piacentini, L. Polastri, G. Polenta, J.-L. Puget, J. P. Rachen, M. Reinecke, M. Remazeilles, A. Renzi, G. Rocha, C. Rosset, G. Roudier, J. A. Rubiño-Martín, B. Ruiz-Granados, L. Salvati, M. Sandri, M. Savelainen, D. Scott, E. P. S. Shellard, C. Sirignano, G. Sirri, L. D. Spencer, R. Sunyaev, A.-S. Suur-Uski, J. A. Tauber, D. Tavagnacco, M. Tenti, L. Toffolatti, M. Tomasi,

T. Trombetti, L. Valenziano, J. Valiviita, B. Van Tent, L. Vibert, P. Vielva, F. Villa, N. Vittorio, B. D. Wandelt, I. K. Wehus, M. White, S. D. M. White, A. Zacchei, and A. Zonca, "Planck2018 results: Vi. cosmological parameters," *Astronomy amp; Astrophysics*, vol. 641, p. A6, Sept. 2020.

[5] D. Baumann, *Cosmology.* Cambridge University Press, 2022.

[6] R. Durrer, "The cosmic microwave background: the history of its experimental investigation and its significance for cosmology," *Classical and Quantum Gravity*, vol. 32, p. 124007, June 2015.

[7] R. H. Dicke, P. J. E. Peebles, P. G. Roll, and D. T. Wilkinson, "Cosmic Black-Body Radiation.," , vol. 142, pp. 414–419, July 1965.

[8] A. A. Penzias and R. W. Wilson, "A Measurement of Excess Antenna Temperature at 4080 Mc/s.," , vol. 142, pp. 419–421, July 1965.

[9] S. Hanany, M. D. Niemack, and L. Page, *CMB Telescopes and Optical Systems*, p. 431–480. Springer Netherlands, 2013.

[10] J. M. Kovac, E. M. Leitch, C. Pryke, J. E. Carlstrom, N. W. Halverson, and W. L. Holzapfel, "Detection of polarization in the cosmic microwave background using dasi," *Nature*, vol. 420, p. 772–787, Dec. 2002.

[11] A. C. S. Readhead, S. T. Myers, T. J. Pearson, J. L. Sievers, B. S. Mason, C. R. Contaldi, J. R. Bond, R. Bustos, P. Altamirano, C. Achermann, L. Bronfman, J. E. Carlstrom, J. K. Cartwright, S. Casassus, C. Dickinson, W. L. Holzapfel, J. M. Kovac, E. M. Leitch, J. May, S. Padin, D. Pogosyan, M. Pospieszalski, C. Pryke, R. Reeves, M. C. Shepherd, and S. Torres, "Polarization observations with the cosmic background imager," *Science*, vol. 306, p. 836–844, Oct. 2004.

[12] A. Explained, "Cosmic microwave background radiation: Definition and history," 2024. Accessed: 2025-07-04.

[13] C.-P. Ma and E. Bertschinger, "Cosmological perturbation theory in the synchronous and conformal newtonian gauges," *The Astrophysical Journal*, vol. 455, p. 7, Dec. 1995.

[14] D. Blas, J. Lesgourgues, and T. Tram, "Class: Cosmic linear anisotropy solving system." `https://github.com/lesgourg/class_public`, 2025. Accessed: 2025-07-06.

[15] H. A. Winther, "Cmb literature database," 2024. Accessed: 2025-06-11.

[16] M. CHEVALLIER and D. POLARSKI, "Accelerating universes with scaling dark matter," *International Journal of Modern Physics D*, vol. 10, no. 02, pp. 213–223, 2001.

[17] P. Callin, "How to calculate the cmb spectrum," 2006.

[18] S. Seager, D. D. Sasselov, and D. Scott, "A new calculation of the recombination epoch," *The Astrophysical Journal*, vol. 523, p. L1–L5, Sept. 1999.

[19] G. Ballesteros and J. Lesgourgues, "Dark energy with non-adiabatic sound speed: initial conditions and detectability," *Journal of Cosmology and Astroparticle Physics*, vol. 2010, p. 014–014, Oct. 2010.

[20] U. Seljak and M. Zaldarriaga, "A line-of-sight integration approach to cosmic microwave background anisotropies," *The Astrophysical Journal*, vol. 469, p. 437, Oct. 1996.

[21] R. M. Sullivan, L. T. Hergt, and D. Scott, "Methods for cmb map analysis," 2024.

[22] A. Zonca *et al.*, "healpy documentation (latest version)," 2025. Accessed: 2025-07-02.

[23] J. Feldbrugge, "Complex evaluation of angular power spectra: Going beyond the limber approximation," 2023.

[24] P. Simon, "How accurate is limber's equation?," *Astronomy amp; Astrophysics*, vol. 473, p. 711–714, Aug. 2007.

[25] N. D. L. of Mathematical Functions, "Gamma function," 2024. Release 1.1.17 of 2024-05-10.

[26] A. Cuyt, V. B. Petersen, B. Verdonk, H. Waadeland, and W. B. Jones, *Handbook of Continued Fractions for Special Functions*. New York: Springer, 2008.